UNIVERSIDADE FEDERAL DO RIO GRANDE DO SUL

PROGRAMA DE PÓS-GRADUAÇÃO EM CIÊNCIA DOS MATERIAIS

Deposition of nickel on polymeric carbon nitride via magnetron sputtering aiming for photocatalytic hydrogen production

Muhammad Rameez Khan Khattak

Master's Thesis

Porto Alegre, September 2024

UNIVERSIDADE FEDERAL DO RIO GRANDE DO SUL

PROGRAMA DE PÓS-GRADUAÇÃO EM CIÊNCIA DOS MATERIAIS

Deposition of nickel on polymeric carbon nitride via magnetron sputtering aiming for photocatalytic hydrogen production

Muhammad Rameez Khan Khattak

Dissertation conducted under the supervision of Prof. Dr. Anderson Thesing and co-supervision of Dr. Lara F. Loguercio, submitted to the Graduate Program in Materials Science at the Universidade Federal do Rio Grande do Sul in partial fulfillment of the requirements for the degree of Master in Materials Science.

Porto Alegre, September 2024

ACKNOWLEDGMENTS

I would like to begin by expressing my deepest gratitude to Almighty Allah for blessing me with the opportunity to pursue a Master's degree in Materials Science at the Federal University of Rio Grande do Sul, Brazil. Without His guidance, none of this would have been possible. I would like to thank the Coordination for the Improvement of Higher Education Personnel (CAPES) for their support through the scholarship, which has made this journey financially feasible.

I am deeply grateful to my supervisor, Prof. Dr. Anderson Thesing, for his unwavering support, guidance, and patience throughout my research. His expertise and encouragement have been vital in shaping my work and helping me to achieve my goals. I also express my special thanks to my co-supervisor, Dr. Lara F. Loguercio.

I would like to express my special thanks to my lab colleagues, especially Hameed, Asif, and Ariadne, for their help during my Master’s at the Laboratory of Nanomaterials for Renewable Energy and Artificial Photosynthesis (NanoREAP). I am thankful to Mr. Silvio Kirst for always being there to assist with any lab-related issues that arise. I also would like to thank to CNANO for the XRD measurement, LAMAS-UFRGS for XPS measurements, CEOMAT-UFRGS for UV-Vis spectroscopy, LCN for SEM, and Dr. Jesum Alves Fernandes from the University of Nottingham for the ICP measurements.

My most significant appreciation goes to my Family, my father, Islam Saeed and my mother, Zeenat Bibi, whose endless love, sacrifice, and encouragement have been the foundation of my success. Their unwavering belief in me has always been my source of strength, and I owe everything to their guidance and support. To my brothers and sisters, thank you for being my constant pillars of support. Your care, encouragement, and faith in me have been invaluable throughout this journey. I am forever grateful for all of you, and your presence in my life continues to inspire and motivate me every day.

LIST OF SCIENTIFIC PRODUCTION

The list of scientific production, including conference papers and a submitted paper is listed below:

- Submitted paper: Surface oxygen vacancies in hierarchical metal oxide nanostructures: optoelectronic tuning in photocatalysis, The Journal of Physical Chemistry C. Date of submission: 07/28/2024. Status: answering referee's.
- Conference paper: Deposição de cocatalisador metálico em nitride de carbono através de magnetron sputtering: potencial candidato para reações de fotocatálise, III MultiMAT, 2024.
- Conference paper: Controlling oxygen vacancies in flower-like SrTiO3 nanostructures through thermal treatment for enhanced photocatalytic activity, SBPMat B-MRS, 2024. Status: accepted.

ABSTRACT

The design and synthesis of artificial photocatalysts with high activity have garnered significant scientific attention globally as a potential solution to the global energy and environmental crisis. Polymeric carbon nitride (CN) has shown considerable potential in the field of photocatalysis due to its unique properties. However, the high recombination rate of photoinduced electron-hole pairs severely limits the photocatalytic efficiency of pristine CN. This study investigates the synthesis and the deposition of nickel (Ni) cocatalysts over CN aiming for photocatalytic hydrogen (H_2) production reaction. The research focuses on understanding the structural, compositional, and optoelectronic properties of CN-Ni systems. CN was synthesized via thermal polycondensation of melamine and subsequently loaded with Ni using magnetron sputtering, with the Ni loading controlled by varying the deposition time (from 0 to 10 minutes). Detailed analyses were conducted using UV-Vis spectroscopy, X-ray photoelectron spectroscopy (XPS), X-ray absorption spectroscopy (XAS), FTIR, scanning electron microscopy (SEM), and X-ray diffraction (XRD). The results indicate that nickel is present in the Ni^{2+} state as NiO_x and $Ni(OH)_x$ species. The deposition induces changes in the chemical environment of CN, particularly in the nitrogen bonding states, which is believed influence photocatalytic performance. This study provides valuable insights into the role of non-noble metal cocatalysts in photocatalysis, demonstrating a promising approach for H_2 evolution via photolysis.

RESUMO

O design e a síntese de fotocatalisadores artificiais com alta atividade têm atraído significativa atenção científica global como uma potencial solução para a crise energética e ambiental mundial. O nitreto de carbono polimérico (CN) tem mostrado considerável potencial no campo da fotocatálise devido às suas propriedades únicas. No entanto, a alta taxa de recombinação dos pares elétron-buraco fotoinduzidos limita severamente a eficiência fotocatalítica do CN puro. Este estudo investiga a síntese e caracterização do CN e sua melhoria através da deposição de cocatalisadores de níquel (Ni) visando a produção fotocatalítica de hidrogênio (H_2). A pesquisa foca em entender as propriedades estruturais, composicionais e optoeletrônicas dos sistemas CN-Ni. O CN foi sintetizado via policondensação térmica de melamina e, subsequentemente, Ni foi depositado usando a técnica de *magnetron sputtering*, com a quantidade de Ni controlado pela variação do tempo de deposição (de 0 a 10 minutos). Análises detalhadas foram conduzidas utilizando espectroscopia UV-Vis, espectroscopia de fotoelétrons de raios X (XPS), espectroscopia de absorção de raios X (XAS), FTIR, microscopia eletrônica de varredura (SEM) e difração de raios-X (XRD). Os resultados indicam que o níquel está presente no estado Ni^{2+} como espécies NiO_x e $Ni(OH)_x$. A deposição induz mudanças no ambiente químico do CN, particularmente nos estados de ligação do nitrogênio, que se acredita que podem influenciar o desempenho fotocatalítico. Este estudo oferece percepções sobre o papel dos cocatalisadores de metais não nobres na fotocatálise, demonstrando uma abordagem promissora para a produção de H_2.

LIST OF FIGURES

LIST OF TABLES

ABBREVIATIONS

CN	Polymeric carbon nitride
H_2	Hydrogen
O_2	Oxygen
H_2O	Water
CB	Conduction Band
VB	Valence Band
e^-	Electron
h^+	hole
GHGs	Greenhouse gases
Co_2	Carbon dioxide
No_x	Nitrogen Oxides
So_x	Sulfur Oxides
PEC	Photoelectrochemical
E_g	Bandgap
HOMO	Highest Occupied Molecular Orbital
LUMO	Lowest Unoccupied Molecular Orbital
e^-/h^+	Electron-Hole
VBs	Valence Bands
CBs	Conduction Bands
HER	Hydrogen Evolution Reaction
OER	Oxygen Evolution Reaction
eV	Electron Volt
CBM	Conduction Band Minima
VBM	Valence band Maxima
E_a	Activation Energy

TEOA	Triethanolamine
φ	Work Function
Ni	Nickel
PVD	Physical Vapor Deposition
CVD	Chemical Vapor Deposition
C	Carbon
N	Nitrogen
O	Oxygen
S	Sulphur
DFT	Density Functional Theory
X	Minutes
λ	Wavelength
B.E	Binding Energy
Ar	Organ
XRD	X-Ray Diffraction
SEM	Scanning Electron Microscopy
UV- Vis	Ultra Violet Visible Spectroscopy
XPS	X-Ray Photon spectroscopy
FTIR	Fourier Transform Infra-Red Spectroscopy
XAS	X-Ray Absorption Spectroscopy

TABLE OF CONTENTS

1. INTRODUCTION

Solar energy utilization has garnered significant attention due to the rising demand for sustainable and clean energy sources. Photocatalytic water splitting is a significant means of storing solar energy as chemical bonds, providing a renewable and carbon-free approach to producing clean hydrogen fuel through artificial photosynthesis.[1,2] In contrast to conventional industrial processes of generating hydrogen, such as steam reforming of natural gases or methane, photocatalytic hydrogen production directly from water utilizing solar-based technology has the potential to become a cost-effective and competitive method for large-scale implementation, provided that the solar-to-hydrogen (STH) conversion efficiency exceeds 10 %.[3] Despite substantial progress in solar-driven water splitting over the past decades, developed photocatalysts' current STH conversion efficiency still falls short of practical requirements. To accomplish industrial-scale and sustainable clean energy production utilizing photocatalytic technology, there is an urgent need to develop highly efficient, environmentally friendly, and economically feasible photocatalysts with exceptional stability.[4]

Polymeric carbon nitride (CN) is an organic semiconductor with a graphite-like structure that has garnered significant attention in research over the last decade due to its extensive range of photocatalytic applications.[5,6] It possesses several advantageous characteristics, such as easy synthesis, tunable properties, affordability, and chemical stability, which make it very promising for photocatalytic applications. In addition, it has emerged as a prominent visible light photocatalyst, similar to the role played by TiO_2 as a benchmark photocatalyst for ultraviolet light.[7,8] In terms of the entire process of water splitting under solar light irradiation, CN has a favorable characteristic where its band edges are appropriately positioned to align with the redox potentials of water. This advantageous feature results in a narrower bandgap, enabling enhanced absorption of visible light.[9]

For efficient and reliable hydrogen (H_2) production, it would be interesting if catalysts are combined with readily available, inexpensive metals that act as cocatalyst, such as Ni. Although Ni-based catalyst systems have been studied recently,[10] there is still lack of information to reveal the nature and structural characteristics of the Ni cocatalyst, as well as the possible structural and bonding situation occurring between the cocatalyst and photocatalyst during photocatalytic HER. Thus, the objective of this study is to investigate the magnetron sputtering method for the deposition of Ni cocatalysts loaded on CN, the

structure and composition of the semiconductor metal cocatalyst system, and its potential application in photocatalytic H_2 production.

2. LITERATURE REVIEW

2.1. WORLD ENERGY OUTLOOK

Global energy consumption has continuously risen due to population increases, economic development, and urbanization. Despite the projected global population reaching around 9.7 billion by 2050, there will be an ongoing rise in the energy demand.[11] Around 80% of the energy consumed worldwide comes from fossil fuels, such as coal, oil, and natural gas.[12]

The combustion of these fuels emits substantial quantities of greenhouse gases (GHGs), predominantly carbon dioxide (CO_2), which contribute to the phenomenon of global warming and alterations in the Earth's climate. Sea levels are rising as a result of global warming, which also results in a decrease in biodiversity and more frequent and extreme weather events.[13] Recently, above-average rainfall was recorded in 147 municipalities in Rio Grande do Sul (southern Brazil), affecting a population of 67,860 inhabitants. The excessive rainfall subsequently extended to the neighboring states of Paraná and Santa Catarina. This prompted the Ministry of Integration and Regional Development of Brazil, alongside federal and state authorities from Rio Grande do Sul, to declare a disaster situation, acknowledging it as one of the region's major climatic disasters. As of June 10, 2024, official data from Rio Grande do Sul, the hardest-hit area, reports 173 deaths, 38 missing persons, 423,486 displaced individuals, 18,854 people in shelters, and 806 injured.[14] This extreme weather shows that severe storms are happening more often and getting stronger because of climate change. The heavy rainfall and its damage are part of a larger pattern of worsening weather due to global climate change. This is one example that makes it clear that we need to take climate change seriously and be better prepared for such severe weather in the future.

The combustion of fossil fuels also emits pollutants, such as nitrogen oxides (NO_x) and sulfur oxides (SO_x), which contribute to air pollution and have significant effects on human health.[15] Furthermore, the unequal allocation of fossil fuel reserves has resulted in geopolitical conflicts and anxieties regarding energy stability.[16] Several countries have begun to invest in renewable energy sources in response to the escalating concerns about the environment and energy security. Clean energy sources that emit little or no greenhouse gases, such as hydroelectric power, solar, and wind power, contribute to lowering the energy sector's overall carbon footprint.[17] Despite that, there is still a significant environment impact

in such energies' sources due the large amount of flood land, for instance, when considering hydroelectric power.

The increasing need for clean, sustainable energy sources has led to technological innovation in the areas of renewable energy distribution, storage, and production. H_2 has become a desirable clean energy carrier because of its high energy density, environmentally friendly nature, and ability to be used in various applications.[18]

2.1.1. Green Hydrogen

Hydrogen is the most basic and common chemical element in the entire universe. The lightest molecule is made up of two linked H atoms (H_2). Under normal conditions, it lacks taste, smell, and color.[19] Water (H_2O) or hydrocarbon molecules are the main molecules on Earth that contain hydrogen. Although H_2 is a gas without color, different color codes have been assigned to it based on its production methods. These include black H_2 (produced from coal), green H_2 (produced from renewable energy sources and water electrolysis), gray H_2 (produced from natural gas), brown H_2 (produced from lignite), and others. The energy sector utilizes these color codes to signify the energy sources, production methods, and key feedstocks used for the manufacture of H_2.[20]

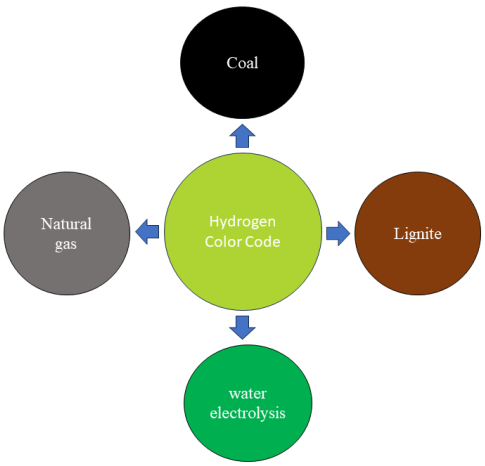

Figure 1 - Different H_2 color codes.

H_2 offers a broad range of advantages. For instance, it plays a crucial role in reducing carbon emissions in global energy sectors by offering carbon-free fuel versatility and serving

as energy storage for the electrical grid. The adaptability of H_2 as a clean fuel, its capacity to power system functions, and its ability to generate heat can be utilized to decrease the carbon intensity of many economic sectors. By 2030, the use of hydrogen technology can potentially eliminate approximately 25% of the worldwide greenhouse gas emissions generated by industries and fossil fuels.[21] Also, it can serve as a highly promising renewable fuel in cars, spacecraft propulsion, airplanes, and electric equipment. However, it is essential to manufacture H_2 from a primary energy source.[22]

H_2 is regarded desirable due to its ability to produce water as a byproduct when burned. The utilization of H_2 does not result in any emissions of GHGs or air pollutants. H_2 possesses the greatest energy density compared to the main fuels utilized today, such as natural gas, gasoline, and diesel. The hydrogen energy content at the higher heating value is 141.8 MJ/kg at 298 K, while the lower heating value of H_2 is 120 MJ/kg at the same temperature. These values are significantly higher than those of most fuels, such as gasoline, which has an energy content of 44 MJ/kg at 298 K.[23–25] H_2 is less dense than both gasoline vapor, air, and rapidly disperses upon release. This allows for rapid spread in the event of a leak. Due to its low density at room temperature, H_2 energy is often measured in kilograms rather than volume.[26]

The most widely used method for producing H_2 is natural gas steam reforming. Due to the substantial emissions of GHGs into the environment, this production technique is not optimal. The objective of the hydrogen economy is to eliminate the reliance on steam reforming of natural gas for H_2 production and instead employ cost-effective, efficient, and sustainable technologies to generate considerable quantities of H_2 from renewable resources.

Water splitting is an efficient method for generating H_2. The process of separating this molecule into its component elements of H_2 and O_2 is called water splitting. Several techniques for water splitting have been proposed, such as photoelectrochemical (PEC) and photocatalytic approaches.[27,28] Photoelectrochemical and photocatalytic water splitting are the two most straightforward, efficient, cost-effective, and environmentally friendly methods for producing H_2.[29]

2.2. SEMICONDUCTOR MATERIALS

In the context of this work, a brief introduction to semiconductor materials is relevant.

Electrical conductivity is a physical property exhibited by certain materials. A material's ability to conduct electricity is characterized by its electrical conductivity. Materials can be categorized into insulators, conductors, and semiconductors based on their capacity to conduct electric current.[30]

The substances that let electrons move through an electric current are known as conductors. The flow is referred to as the material's conductivity. Conversely, materials classified as insulators prevent the passage of electrons through them. Insulators have resistance in the same way as conductors have conductivity.[31] A semiconductor is a material that possesses electrical conductivity that is intermediate between that of a conductor and an insulator. Some examples of semiconductors are silicon and germanium.[32] Adding the proper dopants can result in the production of semiconductor materials, such as n-type and p-type semicondutors.[33]

Semiconductors consist of three primary regions regarding its bands: the conduction band (CB), the forbidden region called band gap (E_g), and the valence band (VB). The electronic structure of a semiconductor can be explained by the band model, which is predicated on the idea of molecular orbitals. When a significant quantity of atoms, each one of them with their respective energy levels, approach one another close enough, the orbitals combine and separate to form two distinct bands, namely the VB and the CB. Figure 2 illustrates the interaction among the electronic orbitals, which results in the formation of the band structure of a semiconductor.

The VB and CB of a semiconductor are derived from the highest occupied molecular orbitals (HOMO) and the lowest unoccupied molecular orbitals (LUMO), respectively.[34,35] At a temperature of 0 K, the VB is the lower energy band that is fully occupied by electrons, while the conduction band CB is the higher energy band that is unoccupied.[36] It is worth noting that the E_g values for semiconductors are narrow enough to allow electrons to move from the VB to the CB through an energy transfer to those materials.[36]

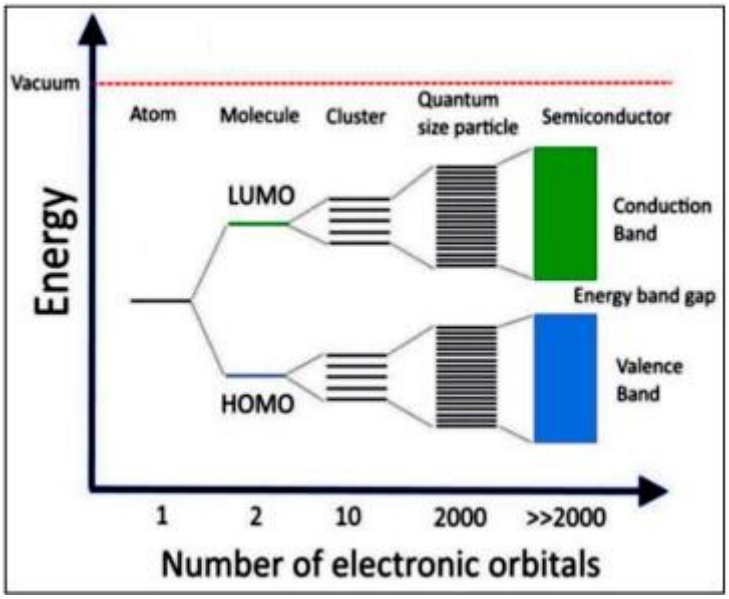

Figure 2 - Illustration representing the band structure of a semiconductor resulting from the interaction of atomic orbitals.[35]

The Fermi level is the energy level in a crystal at a specific temperature when the possibility of an electron occupying any possible energy state is half. An intrinsic semiconductor material refers to a pure crystal without any impurities or dopant atoms. Figure 3 illustrates that holes are the carriers for the VB, whereas electrons are the carriers for the CB. The carrier density can be controlled by introducing dopant atoms, which are carefully chosen based on the semiconductor materials. This doping induces a displacement of the Fermi energy level. An impurity-doped semiconductor with a large number of electrons is referred to as n-type, while if it possesses an excess of holes, it is termed p-type. The schematic band diagrams of materials with intrinsic, n-type, and p-type characteristics are depicted in Figure 3.[37]

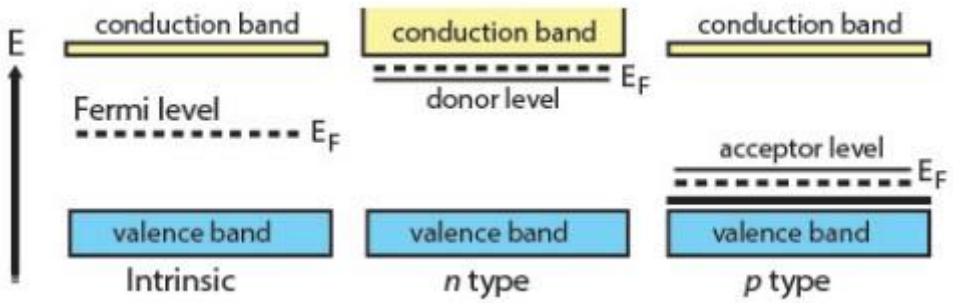

Figure 3 - Schematic energy bands of intrinsic, n-type, and p-type semiconductors.[37]

The band containing electrons is known as the VB. It consists of orbitals with lower energy levels, increasing the electron occupation chance. However, the CB consists of orbitals with higher energy and has lower probabilities of electron occupancy. The difference in energy levels between these two bands is referred to as the E_g energy.

A semiconductor's band structure is a vital component in determining the material's redox capacity and light absorption capabilities, making it an essential parameter for photocatalysis applications. The Fermi function determines the probability of a free electron occupying these bands, which is connected to the system's absolute temperature, the Boltzmann constant, and the Fermi level. The latter refers to the reference energy level of the material, which is the energy level at which there is a 50% chance of electrons being occupied. It is a significant factor in forecasting the material's electrical behavior.[38] The Fermi level in semiconductors is commonly located close to the midpoint of the band gap (E_F = ½ E_g). At temperatures above 0 K, this arrangement facilitates the movement of electrons from the uppermost VB to the lower energy levels of the CB. When a semiconductor absorbs photons with energy equal to or greater than the E_g energy, electrons are excited from the VB to the CB, resulting in the generation of electron-hole (e^-/h^+) pairs as charge carriers. If the charge carriers reach the surface of the semiconductor, the e^-/h^+ couples have the ability to promote redox reactions, and their behavior is directly affected by the locations of the VB and CB. For redox reactions to occur, it is crucial that the charge carriers have a long enough lifespan. On the other hand, electrons can combine with holes, which reduces the effectiveness of semiconductors.[38]

Chemically pure semiconductors exhibit a phenomenon where electrons migrate from the VB to the CB, resulting in empty states in the VB known as holes (h^+). In such situations, conduction happens naturally. Si and Ge are widely recognized as inherent semiconductors. Nevertheless, the utilization of this particular semiconductor has been limited due to its insufficient conductivity. Various approaches have been utilized in this particular situation to improve the electrical characteristics of these substances. One such method is doping, which involves adding impurity atoms into the crystal structure of the semiconductor. These semiconductors, which have been altered by doping, are generally known as extrinsic semiconductors.[38] An intrinsic semiconductor is a kind of semiconductor that is completely free of dopant species. It is sometimes referred to as an undoped semiconductor.

The number of charge carriers is determined by the properties of the material rather than the quantity of impurities present. The quantity of excited electrons and holes in intrinsic semiconductors is equivalent: n = p. This statement remains valid even after the semiconductor has undergone the process of doping, but only if both the donors and acceptors have been doped in equal amounts. In this scenario, the value of n remains equal to p, and the semiconductor retains its intrinsic nature despite being doped.[39]

An extrinsic semiconductor is a semiconductor that has undergone a process called doping during its manufacturing. Doping involves incorporating an impurity or chemical, known as a doping agent, into the semiconductor crystal. This alters the electrical properties of the crystal, distinguishing it from a pure semiconductor crystal, which is also referred to as an intrinsic semiconductor. The presence of foreign dopant atoms within the crystal lattice of an extrinsic semiconductor is mainly responsible for supplying charge carriers that facilitate the transmission of electric current across the crystal.

Two categories of doping agents are used, leading to the formation of two distinct types of extrinsic semiconductors. When a crystal incorporates an electron donor dopant, it releases a mobile conduction electron within the lattice. An n-type semiconductor is an extrinsic semiconductor that has undergone doping with electron donor atoms in order to increase the concentration of negative electrons, which are the primary charge carriers in the crystal. When an atom accepts an electron from the lattice, it creates a vacancy in the crystal where the electron which is actually more appropriately called a hole can pass through like a positively charged particle. This is known as an electron acceptor dopant. A semiconductor that has been doped with electron acceptor atoms is referred to as a p-type semiconductor.[39] This is because the bulk of charge carriers in the crystal are positive holes, as depicted in Figure 4.

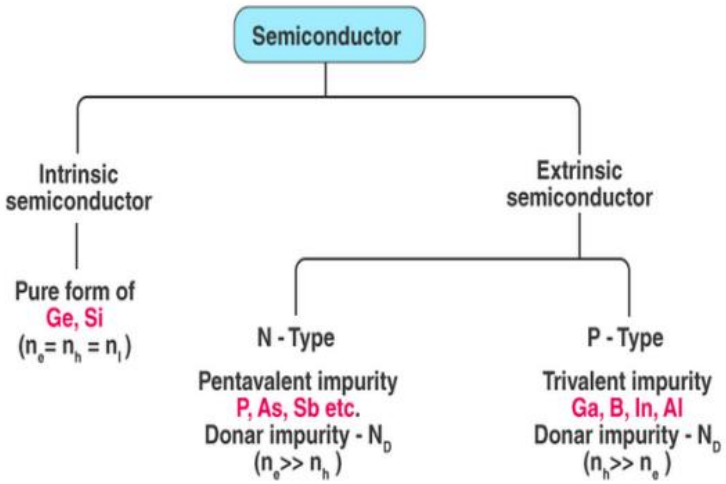

Figure 4 - Classification of semiconductors.[40]

2.3. FUNDAMENTALS OF WATER SPPLITING

The process of water splitting via photocatalysis can be achieved in the presence of a semiconductor and sunlight, producing H_2 and O_2 gas in a 2:1 ratio. This endothermic reaction does not occur spontaneously and requires additional energy ($\Delta G° = 237$ kJ.mol^{-1}), typically solar, to facilitate the multi-electron transfer processes. The overall photocatalytic water splitting reaction (OWS) into H_2 and O_2 is shown in equation 1.

$$2H_2O \rightarrow 2H_2 + O_2 \quad (1)$$

$$2H^+ + e^- \rightarrow H_2 \quad (2)$$

$$2H_2O + 4h^+ \rightarrow 4H^+ + 2O_2 \quad (3)$$

A schematic process of OWS is presented in Figure 5. Under solar irradiation, a semiconductor absorbs photons with energy higher or equal to its bandgap ($h\nu \geq E_{gap}$). As a result, the semiconductor's electrons are excited from the VB to the CB. The initial phase of the photocatalytic process (step 1) involves the generation of excited e^- and h^+. The charge carriers undergo independent diffusion towards the surface of the semiconductor particles (step 2), where they can subsequently engage in the H_2 evolution reaction (HER) and O_2 evolution reaction (OER) on the surface of the photocatalyst (step 3).[41] These reactions are represented by equations 2 and 3.

In order for these two redox reactions to occur, thermodynamic limitations require that the semiconductor's conduction band minimum (CBM) must be positioned at a potential that is more negative than the energy level of H^+/H_2 (0−0.059pH, V versus NHE). Similarly, the valence band maximum (VBM) should be more positive than the energy level of O_2/H_2O (1.23−0.059pH, V versus NHE).[42]

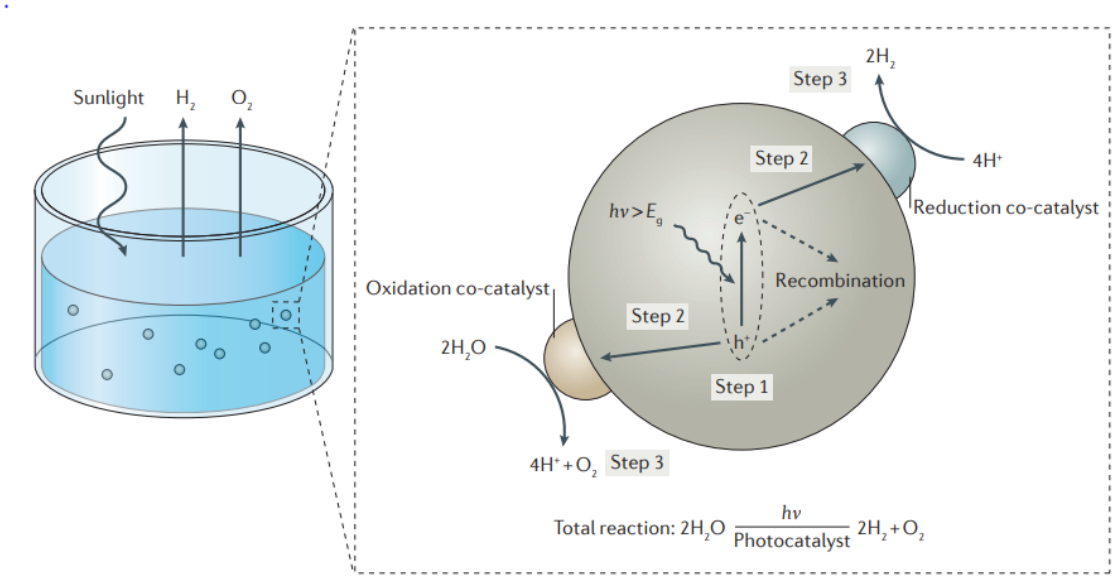

Figure 5 - Schematic illustration of the key steps in the photocatalytic water splitting process.
[43]

The first two stages are influenced by the thermodynamic characteristics of the semiconductors, such as their optical properties, specific surface area, texture, and microstructure.[44] It is evident why most investigations have been focused on the advancement of photocatalytic materials that are stable, effective, and economical. Significant efforts have been made to enhance the light absorption efficiency of semiconductors and optimize the behavior of charge carriers through various chemical strategies, thus improving the OWS performance.[45–47] However, the final stage of the water-splitting process still exhibits a lower reaction rate.

In that sense, the presence of a cocatalyst can be beneficial for increasing final stage efficiency. Under light exposure, the cocatalysts not only act as kinetic accelerators by increasing the rate of gas evolution but also serve as charge trap centers to extract electrons and holes from the photo-excited semiconductors. It reduces the activation energy for the

reaction, expedites the dissociation of hydrogen-oxygen bonds, and consumes the photogenerated charge carriers before recombination. The overall efficiency of the water splitting reaction is also dependent on the type of cocatalysts, amount, size, and composition of it.

Figure 6 illustrates the fundamental principles of thermodynamics which demonstrate that the conversion of one mole of H_2O into one mole of H_2 and half a mole of O_2 under standard conditions results in a Gibbs free energy change of 237 kJ (equivalent to 1.23 eV).[48–50] Also, it shows that activation energy (E_a) is lowered when in the presence of a cocatalyst. In contrast to the half-reaction involving water reduction, the half-reaction involving water oxidation necessitates the movement of four electrons, along with the breaking of O-H bonds and the creation of O-O bonds, and is generally inhibited by a significant activation energy (~700 mV) and the slow kinetics of O-O bond formation.[51] Consequently, the process of water oxidation is frequently more intricate than the half-reaction involving water reduction, rendering it a critical phase in achieving efficient OWS.

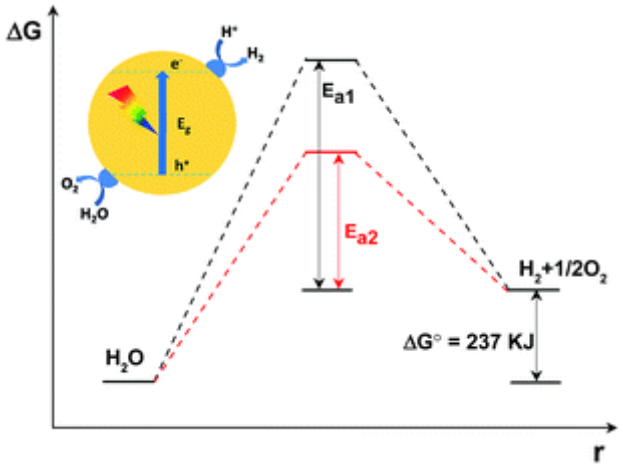

Figure 6 - An illustration of the energy curve for non-sacrificial photocatalytic water splitting using a semiconductor under sunlight. Activation energy E_{a1} is without cocatalysts, whereas E_{a2} is with cocatalysts. r: the redox reaction process; ΔG: the Gibbs free energy change; ΔG^0: standard Gibbs free energy. [52]

As previously indicated, the three stages described of water splitting take place on the system semiconductor-cocatalyst. However, it is essential to understand and optimize reactants that interact with the semiconductor cocatalyst for the optimization of the whole

system. Furthermore, introducing reactants other than water at the reaction medium could alter the redox reaction pathway and diminish the energy obstacle for HER and OER. Such a reactant is called sacrificial agent.

The sacrificial agent system for photocatalytic water splitting is designed for a variety of reasons. Firstly, when considering sacrificial reagents for photogenerated h^+, it is worth noting that their oxidation potential tends to exceed that of water. This in turn increases the driving force for the oxidation half-reaction, leading to a faster consumption of photogenerated h^+ and a reduction in the recombination loss of photogenerated e^-. As a result, the photocatalytic activity for HER is enhanced. Secondly, if pollutants are used as sacrificial reagents, it becomes possible to simultaneously decompose pollutants and generate H_2, thus offering additional benefits. Thirdly, by blocking the effect of photogenerated h^+, the production, transport, and reaction mechanisms of photogenerated e^- can be easily disclosed. The active sites for oxidation reactions could also be tracked using the right sacrificial reagents.[53] In the context of photogenerated h^+ and to facilitate the investigation of the water reduction half-reaction for CN, electron donors like triethanolamine (TEOA), methanol, and ethanol are generally introduced into the system as sacrificial reagents.

2.3.1. Schottky barrier at a semiconductor metal junction

A Schottky junction or Mott-Schottky junction is a region that arises at the interface between a metal and a semiconductor upon their contact.[54] This phenomenon can be observed in a metal/n-type semiconductor configuration. When the two materials are stacked or attached, a difference in their work functions (ϕ) occurs, thereby driving the transfer of free electrons at the interface. Hence, a Mott-Schottky junction becomes manifest at the metal-semiconductor interface.[55]

The work function ϕ is the minimum energy needed to extract an electron from a material at absolute zero temperature (0 K). If the work function of the n-type semiconductor (ϕ_s) is lower than that of the metal (ϕ_m), that is $\phi_m > \phi_s$, electrons migrate from the semiconductor to the metal until the Fermi levels of the materials ($E_{F,s}$ and $E_{F,m}$) equilibrate. This results in band bending and creating a Schottky barrier (ϕ_{SB}).[27] The Schottky barrier enables irreversible charge transport across the interface, leading to charge accumulation or depletion along the contact region.[28]

In the contact region, a continuous shift in the energy band edges of semiconductors occurs due to the electric field between the metal and semiconductor, resulting in the well-known phenomenon of band bending. Precisely, the energy bands bend upward toward the interface when the work function of the metal is greater than that of the semiconductor ($\phi_m > \phi_s$). In contrast, the bend downward when the work function of the metal is lower than that of the semiconductor ($\phi_s > \phi_m$). The direction of band bending can be visualized by considering the electrostatic energy experienced by an electron moving through the interface. The bands bend upward as the electron encounters repulsion from the negatively charged Helmholtz layer in the metal, thus increasing its potential energy. Conversely, when the electron experiences attraction, the bands bend downward.

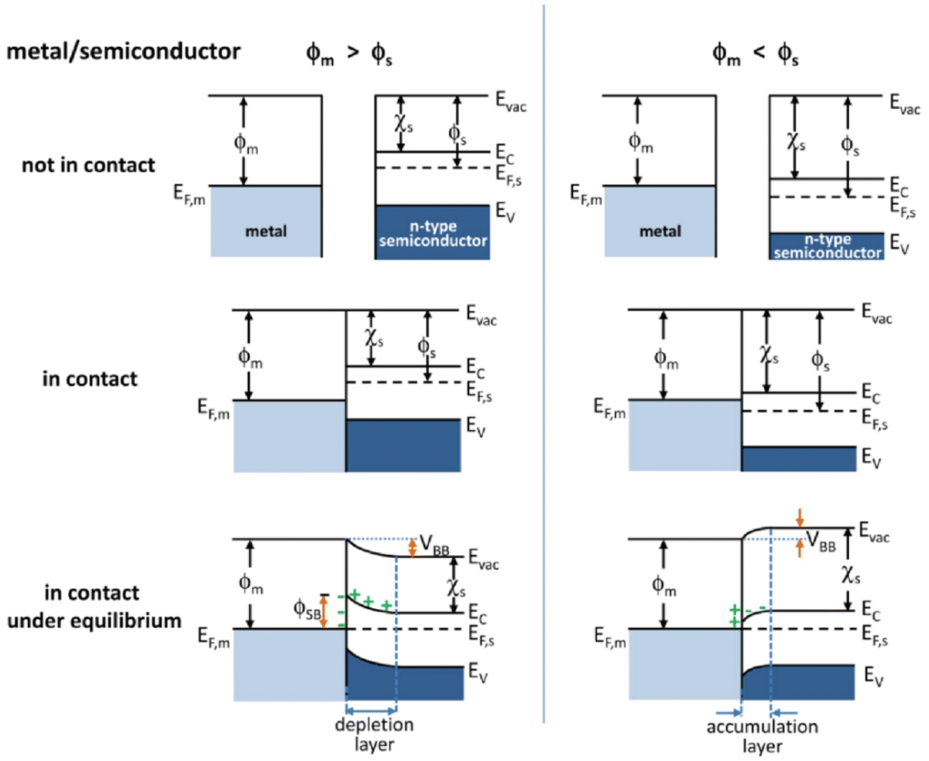

Figure 7- The energy band diagrams show regular metal contacts and n-type semiconductors.

The important variables are the work function (ϕ), electron affinity of the semiconductor (χ_s), Fermi level (E_F), vacuum energy (E_{vac}), conduction band (E_C), and valence band (E_V).[56]

Figure 7 illustrates that the extent of bending of the semiconductor's energy band at the interface is determined by the work function difference (V_{BB}) between the metal and semiconductor (Equation 4):

$$V_{BB} = |\phi_m - \phi_s| \quad (4)$$

In the case where $\phi_m > \phi_s$ for an n-type semiconductor, there is ϕ_{SB} at metal|semiconductor interface. The Schottky barrier height (ϕ_{SB}) is given by Equation 5:

$$\phi_{SB} = \phi_m - \chi_s \quad (5)$$

where χ_s represents the electron affinity of the semiconductor. On the other hand, when $\phi_s > \phi_m$ for an n-type semiconductor, there is no Schottky barrier and the metal-semiconductor contact behaves in an Ohmic manner.[57]

The metal cocatalysts in photocatalysis present several notable benefits, as they serve to enhance the performance of various photocatalysts.[58] The presence of a metal cocatalyst on the surface of a photocatalyst has the potential to promote efficient charge separation due to unidirectional electron transfer, resulting in a significantly increased utilization efficiency of photogenerated electrons, ultimately leading to enhanced photocatalytic performance. [59] Moreover, certain metal cocatalysts demonstrate catalytic activity, serving to enhance specific reactions. For example, in the photocatalytic reduction of H^+ to H_2, metals such as Pt, Pd and Ni function as activators for H_2O, facilitating the reaction and promoting H_2 production.[60]

2.3.2. Metal cocatalyst

Numerous noble metals have been extensively researched as efficient cocatalysts for promoting photocatalytic HER activity. Among these, Pt has been found to be the most effective cocatalyst due to its considerable work function ($\phi = 5.65\ eV$)[61] for electron trapping and low activation energy for H_2 evolution. For instance, when Ru nanoparticles were utilized as the H_2 evolution cocatalyst on CN, the visible light H_2 evolution rate achieved was 2.1 μmol h^{-1}.[62] However, when an equivalent amount of Pt cocatalyst was loaded onto pure CN, the visible light H_2 evolution rate significantly increased to 7.3 μmol h^{-1}, thus highlighting the considerable advantage of Pt in promoting H_2 evolution activity.[62]

The loading contents of H_2 evolution cocatalysts also play a crucial role in photocatalytic activity. At lower loading contents, the activity increases with higher cocatalyst amounts due to the availability of more active sites for redox reactions. Nevertheless, excessive cocatalyst deposition on semiconductor surfaces reduces the number of active sites, shields incident light, and stimulates particle aggregation, all of which adversely impact the cocatalyst's activity. Moreover, high-loading amounts of cocatalysts can

act as charge carrier recombination centers, thereby shortening the lifetime of e^-/h^+ pairs. In conventional practice, noble metal-based cocatalysts, including Pt,[63] Pd,[64] Rh,[62] Au,[65] and Ag,[66] have been preferred for their exceptional H_2 evolution activity, displaying minimal overpotentials and outstanding performance. It is also important to highline that their high cost, toxicity, and limited availability limit their application on a large scale. Therefore, there is a growing need to explore alternative cocatalysts that use abundant and non-toxic elements to achieve sustainable solar energy conversion.[67]

Considering this, exploring cocatalysts based on non-noble metals that have improved characteristics is extremely difficult. Ni has been identified as one of the stable, active, and economically advantageous cocatalysts for HER and CO_2 reduction among the known non-noble metal cocatalysts.[68] According to reports, the deposition of Ni^{2+} onto the CN material has been found to enhance the efficiency of photochemical proton reduction, leading to increased production of H_2.[69] The phenomenon described can be attributed to the effective confinement of electrons within Ni, which facilitates the reduction of H^+ ions to H_2.[70]

Nickel-based cocatalysts, including Ni,[71] NiO,[72] and $Ni(OH)_2$,[73] have gained significant attention for their efficiency in enhancing photocatalytic processes such as water splitting and CO_2 reduction. Their effectiveness is largely due to their unique electronic properties and the specific roles they play in facilitating these reactions.

In photocatalytic systems, metallic nickel (Ni^0) serves as an essential electron transfer agent.[71] Its metallic nature enables it to gather and move photogenerated e^- from the semiconductor to the reaction site efficiently.[74] This lowers e^-/h^+ pair recombination, a common problem that restricts photocatalytic performance. Ni is also very useful in driving the HER, in which hydrogen atoms adsorbed on the Ni surface combine to generate H_2. Ni has a high electrical conductivity and catalytic activity.[75]

NiO is a p-type semiconductor, and when combined with an n-type semiconductor, a p-n junction is formed. Thus, NiO functions as a hole scavenger, providing a complementary function.[76] NiO can capture photogenerated (h^+) from the semiconductor during the photocatalytic process, preventing electron-hole recombination and thereby increasing overall photocatalytic efficiency. [74] On the other hand, $Ni(OH)_2$ is an important cocatalyst that facilitates photoelectron transport in photocatalytic systems, thereby enhancing HER.[73] When combined with a semiconductor, it provides active sites for proton adsorption and reduction. Acting as a mediator for electron transport, $Ni(OH)_2$ possesses unique redox properties that

allow it to undergo reversible oxidation to NiOOH during the photocatalytic process.[77] This redox cycling between $Ni(OH)_2$ and NiOOH is crucial for maintaining a continuous flow of photogenerated (e^-) to the reaction sites, reducing e^-/h^+ pair recombination, and ultimately boosting the overall efficiency of H_2 evolution. [78]

2.3.3 Sacrificial agent in photocatalysis

One of the most significant drawbacks of using photocatalysis for water breakdown is that the pure water method is typically very ineffective or nonexistent. This is due to the fact that the process of reducing and oxidizing water occurs simultaneously and involves a complex reaction with multiple steps, requiring the transfer of four electrons.

Utilizing sacrificial molecules as electron donors can significantly enhance H_2 production.[79] This is because these molecules scavenge holes and effectively decrease charge carrier recombination. Moreover, since O_2 is not generated, the reverse reaction to make water is inhibited, leading to an enhanced H_2 output and eliminating the need for a following gas separation step. It is important to mention that the production of H_2 can be decreased by other reduction processes that occur when the sacrificial reagents are oxidized.[80]

Recently, there has been a concentrated effort in scientific study to create photocatalyst materials that can split water using visible light. Nevertheless, all these photocatalyst systems exhibit their highest level of activity when sacrificial reagents are present. The direct electrolysis of water to produce H_2 and O_2 is inefficient due to the rapid reverse reaction. However, the addition of a sacrificial agent, which acts as a reducing agent, can enhance efficiency. This sacrificial agent facilitates the reduction of water by the photoelectrons from the conduction band.

Methanol and ethanol are types of sacrificial substances frequently employed in photocatalytic water splitting.[81–83] Kumaravel et al.[84] investigated various sacrificial agents, such as glycerol, ethanol, lactic acid, and glucose, and their function in the photocatalytic processes for hydrogen production. The efficacy of the photocatalytic process is greatly influenced by features of the sacrificial agent, such as polarity, electron donating capacity, and chemical affinity towards the photocatalyst surface.[81]

According to Wang et al., methanol and TEOA were shown to be the most effective sacrificial agents in generating hydrogen when TiO_2 and CN were used as photocatalysts.[85] TEOA exhibits exceptional efficacy in removing oxidizing species that are formed on the

surface of CN when it absorbs light.[86] The mechanism of photocatalytic H_2 generation over CN was determined through the conducted analyses. Under simulated solar light irradiation ($hv \geq Eg$), the (e^-) in the VB of CN are excited to its CB, resulting in the formation of photogenerated (h^+). The CB (e^-) can efficiently migrate to the surface of CN. Ultimately, the (e^-) are employed to catalyze the reduction of H^+ ions, resulting in the production of H_2. Simultaneously, the vacancies (h^+) in the VB interact with the hole scavenger (TEOA) to generate an oxidation product ($TEOA^+$), thereby limiting the recombination of light-induced charge carriers.[86,87]

2.4. SEMICONDUCTORS FOR WATER REDUCTION

Various semiconducting materials have been extensively researched and utilized as photocatalysts for HER from water. Our focus will be on the most significant classes of photocatalytic materials, which include metal oxides (e.g., TiO_2, Nb_2O_5, WO_3), metal sulfides (e.g., CdS, MoS_2, ZnS), and nitrides (e.g., CN, β-Ge_3N_4).[88] To maximize solar energy utilization, it is crucial to develop a highly efficient photocatalyst that can split water under visible and/or near-infrared light ($\lambda > 400$ nm), considering that UV light accounts for only 4 % of the total solar energy. Figure 8 represents a schematic diagram of the band structures for some photocatalysts used in water splitting reactions.

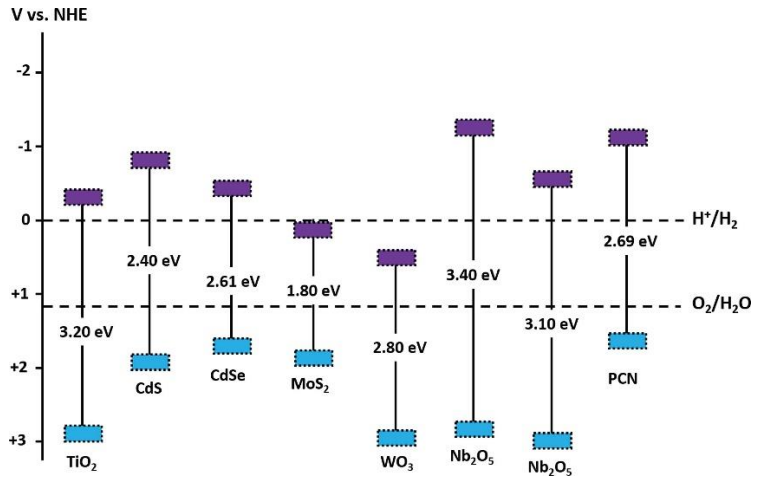

Figure 8 - The schematic illustration shows the band structures and potentials of several semiconductor photocatalysts used in water splitting.[88]

However, producing practical solar H_2 has been a challenge, particularly with UV light, where the maximum Solar to hydrogen (STH) efficiency theoretically reaches only 3.3 %, even at 100 % quantum yield.[89] This efficiency value is inadequate for practical application. Until recently, only a few metal chalcogenides and oxides, such as CdS and WO_3, had shown activity under visible light.[90,91] Certain metal chalcogenides, as CdS and CdSe, have a band gap that allows them to absorb visible light, with CBM and VBM at potentials suitable for HER and OER. Regrettably, they lack stability under water-splitting conditions, as S^{2-} and Se^{2-} anions are more susceptible to oxidation than water, causing self-oxidation of the CdS or CdSe catalyst.[92] Conversely, WO_3 is stable and active under visible light for O_2 evolution, but its CBM is at a more positive potential than that required for the reduction of H^+ to H_2, making H_2 production challenging.[90] CN, however, demonstrates an excellent band structure and remarkable stability. Nevertheless, it suffers from poor quantum efficiency due to its high recombination rate of photogenerated charge carriers, limiting its overall performance as a photocatalyst.

2.4.1. Polymeric carbon nitride

CN are compounds including carbon and nitrogen as primary elements, that have a general chemical formula C_xN_y.[93] CN is the oldest synthetic polymer.[94] The research on it has a history dating back to 1834. Berzelius and Liebig, along with other researchers,[95] successfully created a substance called "melon" via CN bonding. In 1922, Franklin offered the idea of C_3N_4 and suggested that this compound may be produced from a precursor that contains amino carbonic acid.[96] In 1937, Pauling and Sturdivant accurately determined that the fundamental composition of CN consists of tri-s-triazine units.[97] According to Redemann and Lucas et al,[98] CN can be classified as a tri-amino-tri-s-triazine-based polymer that possesses the properties of melon and graphite. During the early 1990s, β-C_3N_4, a material with a sp^3 structure, high hardness, bulk modulus, and a structure similar to that of a diamond, gained significant interest from numerous researchers.[99]

In 2009, Wang and Antonietti et al. made a significant discovery in carbon nitride materials, particularly graphitic carbon nitride (CN). They investigated CN as a metal-free organic semiconductor photocalatyst for the purpose of splitting water into hydrogen under sacrificial conditions.[100] This finding challenged previous beliefs about CN properties. This

work is significant as it revolutionized the field of photocatalysis by introducing metal-free organophotocatalysis and establishing carbon nitrides as a pivotal component.[101]

Due to its exceptional intrinsic optical properties, including high photo-absorption and photo-responsiveness, energy storage, semiconductive character, thermal and chemical stability, CN is a relatively new type of carbon material, which is attracting a lot of attention from researchers. Its optical band gap energy is approximately 2.7 eV. It contributes to improving their energy storage, photocatalytic, field emission, and carbon capture capabilities because of their narrow band gap.[102–106]

Furthermore, CN is a type of graphite analogue that has layered van der Waals structures. Rather than C-C bonds, each of its layers contains strong covalent C-N bonds. It has a nitrogen-substituted graphite network composed entirely of π-conjugated sp^2 hybridized carbon and nitrogen atoms. There are two different condensation states demonstrated on the CN networks, which are (i) heptazine/tri-s-triazine units (Figure 9a) and (ii) s-triazine units (Figure 9b).[107]

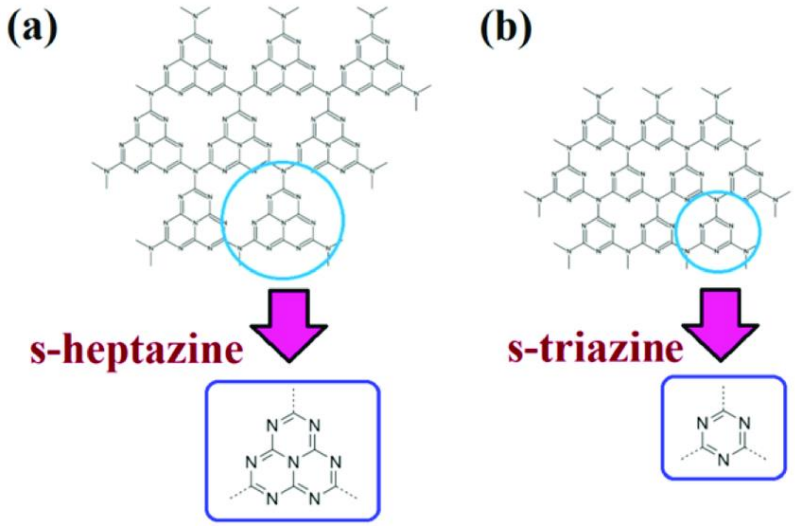

Figure 9 - (a) tri-s-triazine (heptazine) and (b) s-triazine structures of CN.[108,109]

Various methods are available for synthesizing CN, including physical vapor deposition (PVD), chemical vapor deposition (CVD), solvothermal, thermal condensation, and microwave irradiation.[110] Among the various synthesis methods, thermal condensation is

widely accepted for its simplicity. Usually, the nitrogen-rich species used for the thermal polycondensation are affordable organic precursors. Figure 10 displays the molecular structures of various precursors, including urea, thiourea, melamine, cyanamide, dicyandiamide. It also describes the most likely range of temperature that precursor will become as C_xN_y after thermal polycondensation.[111]

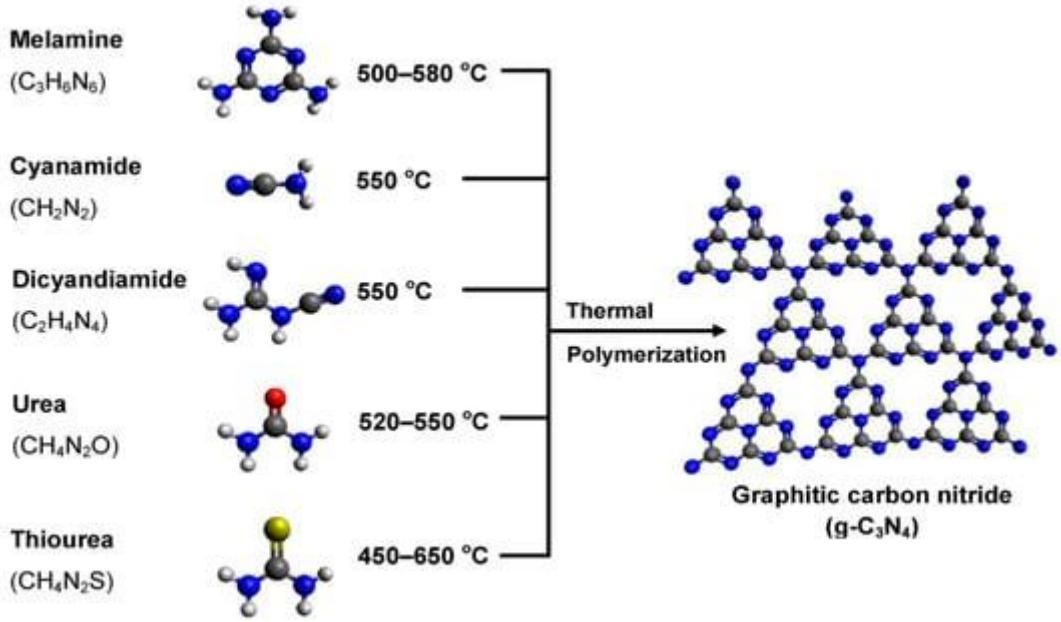

Figure 10 - Scheme of several CN precursors undergoing under thermal polymerization to obtain CN.[112] The black, blue, white, red, and yellow circles stand for C, N, H, O, and S atoms, respectively.

The thermal decomposition transformation for each precursor may follow distinct polyaddition and polycondensation mechanisms but with an equivalent stage of melamine production. For instance, Wang et. al.[113] reported that cyanamide molecules undergo condensation to dicyandiamide and subsequently to melamine (aromatic block) within the temperature range of 200 – 235 °C. At temperatures above 300 °C, the intermediate species remain unchanged and proceed to produce the final CN structure, regardless of the initial precursor. The suggested thermal polycondensation mechanism for the specific example of melamine is seen in Figure 11. It is evident that the process of pyrolysis of melamine causes self-condensation, which generates the melam and melem compounds at a temperature of 320

°C. While the ongoing condensation produces the necessary intermediates, a deamination step occurs through heat reaction. Once melam and melem have sufficiently developed and the temperature exceeds 390 °C, the melon structure becomes visible. Finally, at a temperature of 520 °C, the crystalline phases of CN emerge, resulting in the production of tri-s-triazine and s-triazine based CN.[111] Interesting, according to theoretical calculations, the tri-s-triazine becomes unstable at roughly 600 °C, whereas the polymeric CN undergoes decomposition at 700 °C.[114] Considering the difficulty of conducting in-situ measurements with XRD equipment and the presence of ammonia (corrosive gas) released in different steps, there is a debate in the research community about whether the existence of these intermediates can be experimentally proven by crystallography. Nevertheless, this model remains the most widely accepted postulated process for thermal polycondensation.[111]

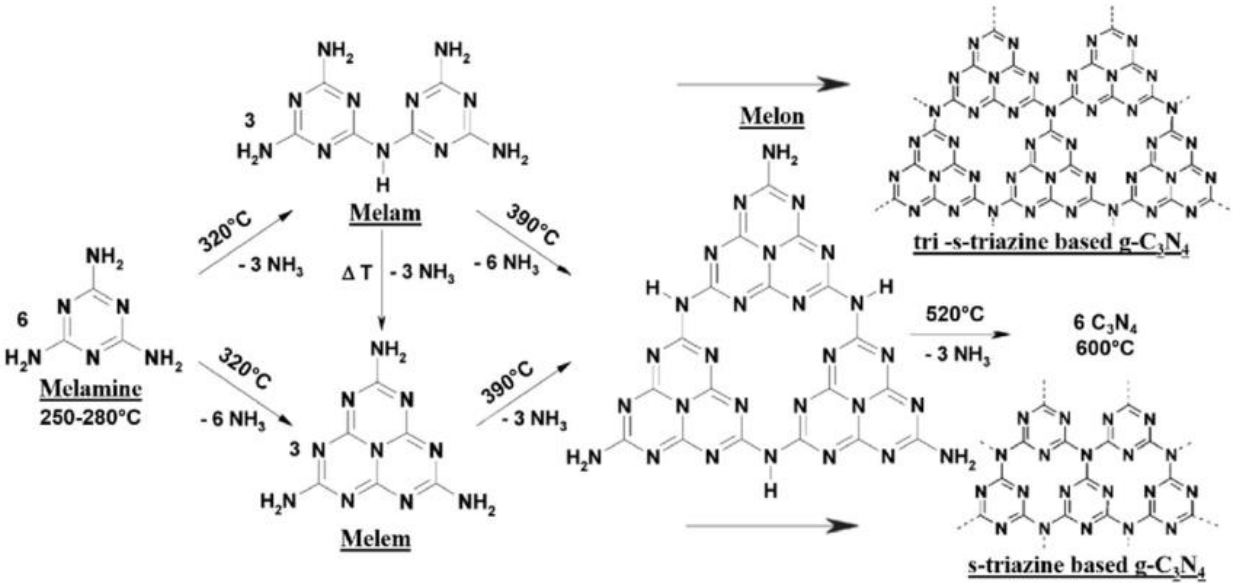

Figure 11 - Thermal polycondensation mechanism of melamine.[114]

To clarify the reaction pathway with greater details, Thomas et al.[110] determined the polyaddition and condensation processes using the ab initio approach. They have shown, using density functional theory (DFT) with a cut-off at 550 eV, that the cohesive energy of the thermal polycondensation of melamine rises during the formation of melem. Melamine and melem are classified as molecular crystals because of their robust covalent bonds within the molecular units, together with their weak interactions. A highly similar chemical route has

been verified, exhibiting the same intermediates as depicted in Figure 11. Therefore, calculations revealed that the morphology of the melon chain is determined by a competition between the energy conservation achieved by extending the π-electron system into a linear chain and the repulsive forces between the lone pair of electrons located on the nitrogen atom positioned at the interfaces. Upon the formation of the CN linear chain, it retains a significant distortion caused by the contact of many nitrogen atoms on the tri-s-triazine edges, which aim to optimize their distance and position.[110,111] Additionally, Kroke et. al.[115] conducted a DFT analysis that verified the thermodynamic stability of the tri-s-triazine based structure to be 30 $kJ.mol^{-1}$ higher than that of s-triazine. As a result, it is considered the most widely accepted unit for CN.

Due to its improved performance and environmental friendliness, it has been used in a variety of fields, including photocatalysis, sensing, and photovoltaics.[116] Photocatalytic materials based on CN demonstrate the ability to effectively eliminate pollutants from the environment through a synergistic process including both adsorption and photocatalysis. As a result, these materials find extensive use in the degradation of pollutants.[117] In the field of photovoltaics, this material possesses a comparatively narrow energy band gap of ~ 2.7 eV. This characteristic enables it to effectively absorb a greater amount of light, so facilitating a heightened rate of photocharge creation. Consequently, a larger number of electrons will be accessible in the CB, thereby facilitating the propulsion of photoreactions.[118] CN-based materials provide several advantageous characteristics, including notable sensitivity and selectivity towards analytes, a substantial surface area, and exceptional chemical stability, which have been widely acknowledged in the field of sensor technology.[119]

Researchers have explored various methods, such as doping and forming heterojunctions with other materials like metal oxides, metal sulfides, noble metals, and carbonaceous nanomaterials, to enhance the performance and modulate the properties of CN in order to decrease recombination rate of photogenerated charge carriers.[120] In that sense, the use of inexpensive metal cocatalysts presented a promising blueprint in photocatalysis owing facile and flexible synthesis methods, abundant varieties, and excellent catalytic performance.[121,122]

3. AIM AND OBJECTIVES

The main goal of this work is to obtain a nanocomposite of nickel and polymeric carbon nitride to apply for hydrogen production. The study aims to investigate the structure and composition of the semiconductor cocatalyst system and correlate these characteristics with the photocatalytic production of green hydrogen.

The objectives to be achieved are described as follows:

- Obtainment of CN;
- Loading of Ni cocatalyst on CN using magnetron sputtering;
- Influence of the Ni amount over structure, composition, optoelectronic properties;
- Investigation of structure, composition and optoelectronic properties of CN-Ni.

4. MATERIALS AND METHODS

4.1. MATERIALS

All chemicals were used without any further purification. Chemicals are described as follows: Melamine (Sigma-Aldrich, 99 %), triethanolamine (TEOA, Sigma-Aldrich, 99%), and Nickel target (AJA, 99.999 %). Deionized water was used when needed.

4.2. METHODS

4.2.1. Synthesis of polymeric carbon nitride

Before the reaction, the crucible was cleaned with soap, deionized water and dried it in the oven at 70 °C. Afterwards, clean procedure was completed by heating up to 1000 °C for 1 h in an open atmosphere. Melamine was used as a precursor for CN. For the reaction, 10.0 g of melamine was grounded in a mortar and pestle. The ground powder of melamine was put into a crucible (3.8 cm height and 6.3 cm in diameter) in the middle of the static oven (Sanchis). Figure 12 shows the crucible and oven used for the reaction. The reaction was performed with the heating rate of 3 °C.min^{-1} up to 550 °C for 3 h in an open atmosphere. The sample was left to cool to room temperature. The resulting yellow sample was obtained and ground into powder named CN.

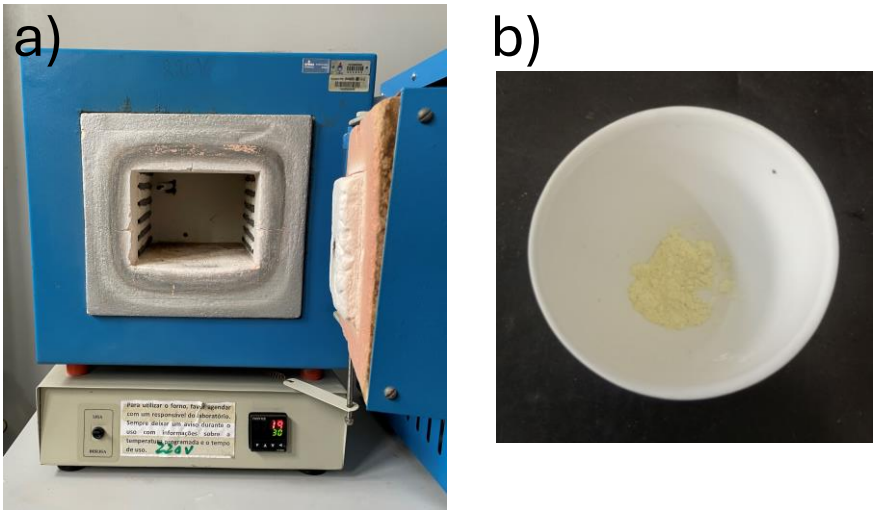

Figure 12 - (a) Static oven and (b) crucible used for the synthesis of CN.

4.2.2. Deposition of cocatalyst

The magnetron sputtering system was used to deposit Ni on CN. The powder sample (0.17 g) was inserted into the main chamber inside the sample holder, and then evacuated to 5.10^{-3} mbar. Afterwards, the turbomolecular pump was used to further decrease the pressure up to 3.10^{-5} mbar. An argon pressure of $1.7.10^{-3}$ mbar was stabilized in the main chamber. The magnetron sputtering gun was turned on for 2.5, 5.0, 7.5, and 10.0 minutes of deposition with a power of 20 W. The sample holder oscillation frequency was set to 28 Hz with a 1.0 A current. After deposition, the main chamber was vent with Ar for sample removal and storage. The samples were named CN-Ni X, where X represents the deposition time in minutes.

4.2.3. Characterization

UV-Vis spectrometry was preformatted in a Cary 5000 using an integrating sphere at the range 200 to 800 nm. The band gap energies were obtained by the diffuse reflectance spectra using Kubelka-Munk function (equation 6):

$$KM(R) = \frac{(1-R)^2}{2R} \qquad (6)$$

Infrared spectroscopy was perfomed in an FTIR-ATR Bruker Alpha-P whitin the range of 500 to 4000 cm^{-1}.

The X-ray photoelectron spectroscopy (XPS) was collected in an Omicron Gmbh equipment using Al Kα radiation (1486.6 eV). The C 1s signal was used for energy calibration at 284.8 eV. The data were processed using CasaXPS software, applying a Shirley background, a GL(30) function for all components, and maintaining the same FWHM when in the same atomic orbital.

X-ray absorption spectroscopy (XAS) measurements were performatted at IPE beamline at Sirius synchrotron light source, Brazil. The C K-edge, N K-edge and Ni $L_{3,2}$-edge spectra were collected in total fluorescence yield (TFY) mode (step size of 0.1 eV and acquisition time of 0.1 s/step). The data were processed at ATHENA software.

The X-ray diffraction (XRD) measurements were obtained on a Rigaku diffractometer with a CuKα radiation (λ=1.54 Å) in the 2θ range of 10 to 70°. The d spacing were calculate by the using Bragg's equation (Equation 7):

$$d = \frac{n\lambda}{2sin\theta} \quad (7)$$

The amount of Ni loaded on CN was quantified by ICP-OES using a Perkin-Elmer Optima 2000 spectrometer, in triplicate measurements with 10 mg of the catalyst digested in aqua regia (5 mL).

Scanning electron microscopy (SEM) images were obtained on a Jeol JIB 4500 microscope with an acceleration voltage of 15 kV. The powder was placed on a carbon tape, directly attached to the stub without any metal coverage.

5. RESULTS AND DISCUSSION

The results obtained throughout this work will be presented and discussed in this section. Initially, the synthesis process of CN via thermal polycondensation of melamine will be addressed (section 5.1), followed by the deposition of Ni using magnetron sputtering (section 5.2). Then, using the optimized conditions, the optical, structural, and compositional properties of the samples will be analyzed and discussed (section 5.3). Next, the section regarding the potential of photocatalysis for the samples will be presented (section 5.4).

5.1. OBTAINEMENT OF CARBON NITRIDE

The synthesis of carbon nitride can be achieved using various approaches, some of which are discussed in section 2.4.1. The process primarily relies on the thermal polycondensation of a nitrogen-rich precursor. Mechanistically, the transformation of various precursors into CN is generally a multistep process. It begins with the polymerization and polycondensation of melamine, leading to the synthesis of melam. Subsequently, a rearrangement of melam occurs, forming the tri-s-triazine-based compound known as melem, which takes place at approximately 390 °C. Melem then undergoes further condensation, resulting in the formation of melon polymer. Finally, at around 520 °C, the melon polymer condenses further to create a polymeric network known as polymeric carbon nitride.

This brief discussion highlights the numerous variables that can influence the material's synthesis. These include the precursor molecule used, the type and size of the crucible, whether or not the crucible is covered during thermal treatment, the thermal treatment environment, the ramping stages, and the heating rate. Choosing the appropriate experimental parameters for a desired application is, therefore, not a straightforward task.

Before proceeding with this work, it is worth mentioning that several of these parameters were tested in collaboration with coworkers in the group. In fact, ongoing research is currently investigating the effect of heating rate on CN synthesis and its potential relationship to photocatalysis, as well as the influence of the crucible during synthesis. While it is recognized that the aforementioned parameters significantly influence the material, the goal of this thesis is to study the CN semiconductor system with different loadings of Ni cocatalyst. Therefore, a standard cylindrical crucible and a heating rate commonly used in the literature have been chosen.

5.2. MAGNETRON SPUTTERING SYSTEM

The magnetron sputtering system in our laboratory is a homemade machine. Since the beginning of this thesis, we have made changes and improvements in the equipment aiming to make a faster and high-reproducible process. Despite being time-consuming, all those changes are now done, and the equipment is ready to use.

Basically, the system consists of three chambers: the main chamber, the turbomolecular pump chamber, and the plate chamber (Figure 13 a). The plate chamber allows for partial or complete closure of the turbomolecular pump entry and is equipped with an auxiliary mechanical pump (Auxiliary 1). A second auxiliary pump (Auxiliary 2) is installed beneath the turbomolecular pump. This setup enables us to maintain a constant Ar pressure during depositions.

The main chamber features a removable side for inserting the sample holder, with the substrate positioned below the magnetron sputtering source, which is mounted at the top of the chamber (Figure 13b). A movable steel plate (shutter) is located between the sample holder and the substrate. One distinguishing feature of this system compared to conventional sputtering machines is the powder sample holder. An adjustable vibration mechanism is available for use with powder samples. By controlling the alternating current's frequency and intensity on a coil, we can cause the sample holder to vibrate given the alternating magnetic field, allowing the powder to move continuously during deposition. This is extremely important because ensures uniform deposition around the semiconductor nanoparticles.

Interestingly, this also means that each sample needs to be tested individually before deposition. For instance, when using CN or $SrTiO_3$, the vibration conditions can vary significantly due to the textural properties of the materials. Empirically, this means that the weight of the sample, the current, and the frequency need to be optimized prior to the deposition. In this thesis, the optimized conditions for CN were 0.17 g, at 28 Hz and 1.0 A. Under these conditions, we visualize the maximum possible amount of powder vibrating without spillover.

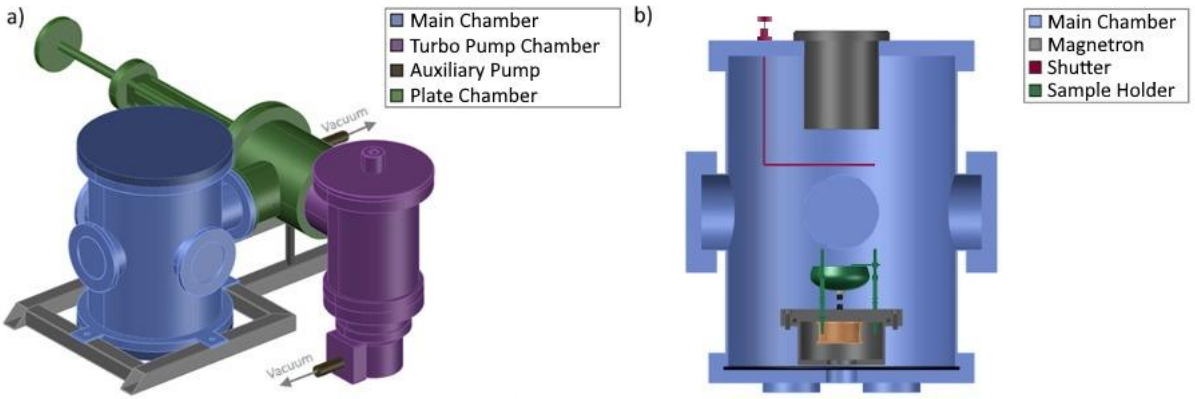

Figure 13 - (a) Equipment used for magnetron sputtering, b) interior of the main chamber.

Once the sample holder conditions were establish, we proceeded with the deposition of Ni using the power of 20 W. Using different deposition times, we control the amount of Ni onto the samples. To determine the amount of Ni deposited on CN, we used the ICP-OES technique. The results for CN, CN-Ni-2.5, CN-Ni-5, and CN-Ni-7.5 are shown in Figure 14.

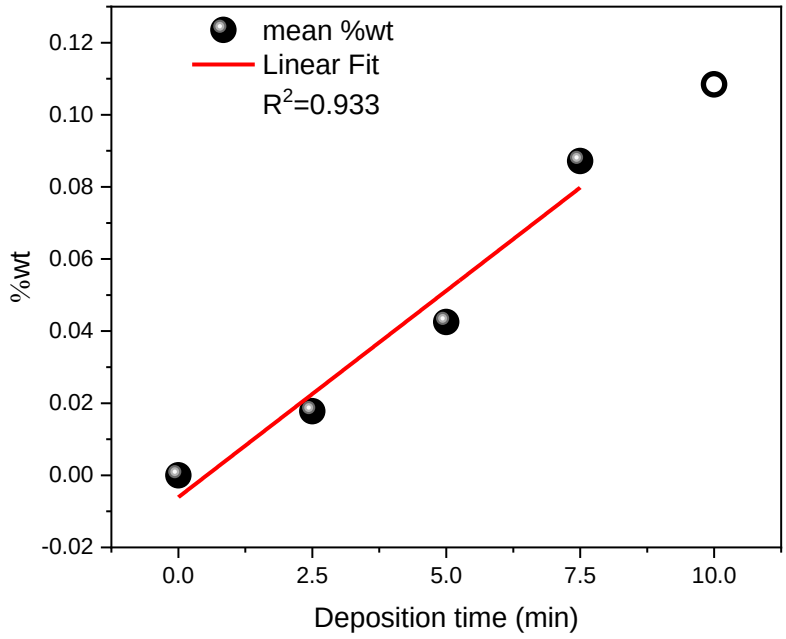

Figure 14 - ICP-OES results of Ni. The open circle is the value estimated using Equation 8 for deposition time of 10 minutes.

A clear linear relationship between the Ni %wt and deposition time is observed, with the power fixed at 20 W and the sample holder maintained at 28 Hz and 1.0 A using 0.17 g. From the linear fit, we can write an equation to estimate the amount of Ni deposited for other deposition times, as follows:

$$\%wt = -0.00608 + 0.01145(x) \quad (8)$$

Where x represents the deposition time in minutes. For the sample CN-Ni-10.0, the calculated Ni %wt is indicated in Figure 14 as an open circle. In addition, the slope of the linear equation confirms a deposition rate of 0.01145%wt/min, indicating a relatively low deposition rate. This allows for precise control over the amount of Ni deposited on the samples. Finally, the results indicate the range of Ni amount from 0.018 to 0.11 %wt. Considering the procedure used here, we can also use the results from Equation 8 and the described deposition conditions for other projects that are based on CN samples.

5.3. PHYSICAL-CHEMICAL PROPERTIES OF THE PHOTOCATALYST

Digital images of the samples obtained are shown in Figure 15. They all have a yellow color, with no clear color change after Ni deposition. Also, the aspects of all of them are visually the same.

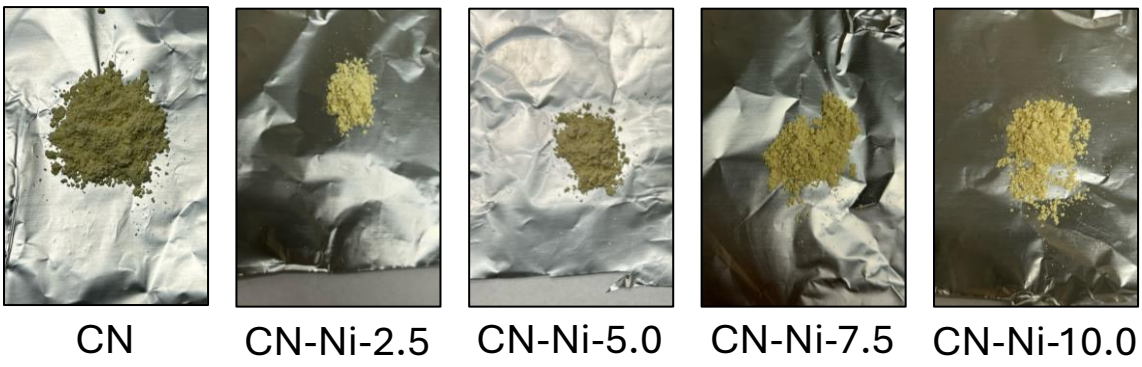

Figure 15 - Digital image for CN-Ni samples.

SEM was used to evaluate the morphology of the samples prepared in this work. The SEM images presented on the left of Figure 16 were obtained using secondary electrons detector, and show a crumpled morphology, with no apparent changes across the different samples. The expected layered structure may promote strong van der Waals interactions between adjacent layers, forming compact structures.

By using backscattered electrons, we can differentiate atoms with distinct atomic numbers, such as C/N from Ni. On the right side of Figure 16, no evident Ni particles were observed in the images obtained with the backscattered electron detector. Given that the presence of Ni is confirmed by ICP-OES (and by the following discussion in this section), this suggests that the size of the Ni particles is beyond the limit of the equipment used. Therefore, suggesting the Ni species are nanoparticles.

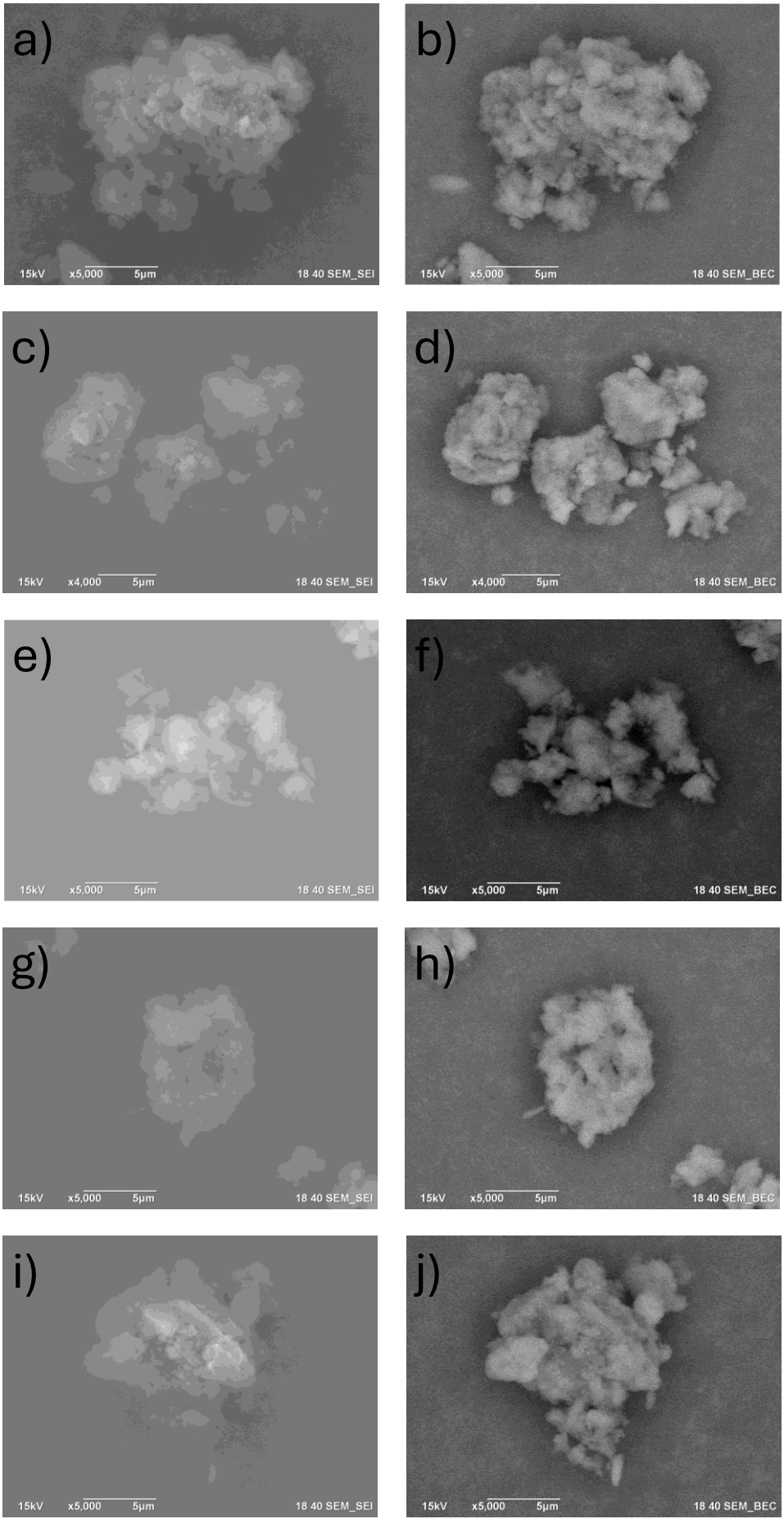
a)
15kV x5,000 5µm 18 40 SEM_SEI
b)
15kV x5,000 5µm 18 40 SEM_BEC
c)
15kV x4,000 5µm 18 40 SEM_SEI
d)
15kV x4,000 5µm 18 40 SEM_BEC
e)
15kV x5,000 5µm 18 40 SEM_SEI
f)
15kV x5,000 5µm 18 40 SEM_BEC
g)
15kV x5,000 5µm 18 40 SEM_SEI
h)
15kV x5,000 5µm 18 40 SEM_BEC
i)
15kV x5,000 5µm 18 40 SEM_SEI
j)
15kV x5,000 5µm 18 40 SEM_BEC

Figure 16 - SEM images of (a-b) CN, (c-d) CN-Ni-2.5, (e-f) CN-Ni-5.0, (g-h) CN-Ni-7.5, and (i-j) CN-Ni-10.0. The left side shows the images obtained using secondary electrons, while the right side shows the images obtained using backscattered electrons.

The EDS elemental mapping results are presented in Figure 17. These images clearly show that C, N, and O are uniformly distributed across the samples. The presence of Ni could not be detected (the counting was too low), corroborating with SEM images using backscattered electrons. This is attributed to the low amount of metal in the samples.

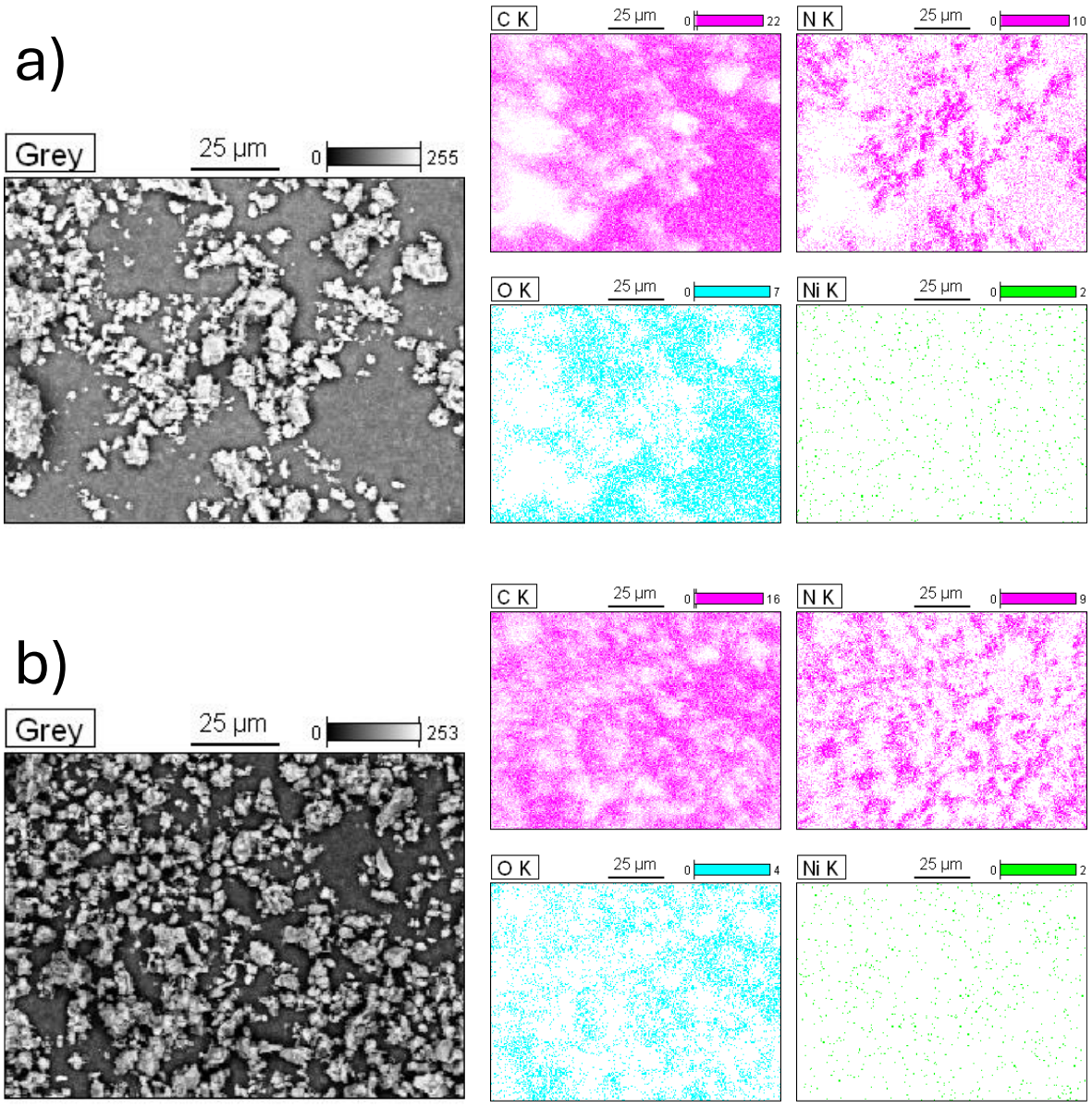

Figure 17 - EDS element mapping images of (a) CN and (b) CN-Ni-10.0.

The diffuse reflectance spectra obtained (Figure 18a) was used to construct Kubelka-Munk plots (Figure 18b). The optical band gap of CN-Ni samples was obtained from UV-Vis spectroscopy, and the results are presented in Figure 18. Using the Kubelka-Munk plot, one can observe a dramatic drop from 3.1 to 3.4 eV. This abrupt drop corresponds to the energy region where electrons were excited from VBM to CBM. For CN, VB are mainly composed of atomic orbitals of N atoms, and the CB have the atomic orbitals of C + N atoms. According to the literature, for CN it's an indirect transition.[123] By the linear extrapolation of the Kubelka-Munk plot, the optical band gap is calculated as ~2.77 eV for all samples. Those are similar values of band gap energies for samples with CN.[123]

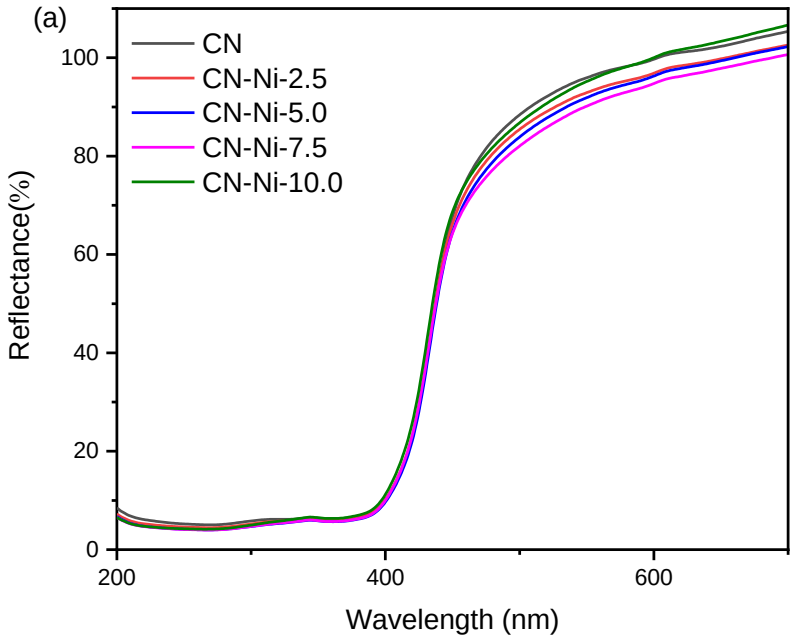

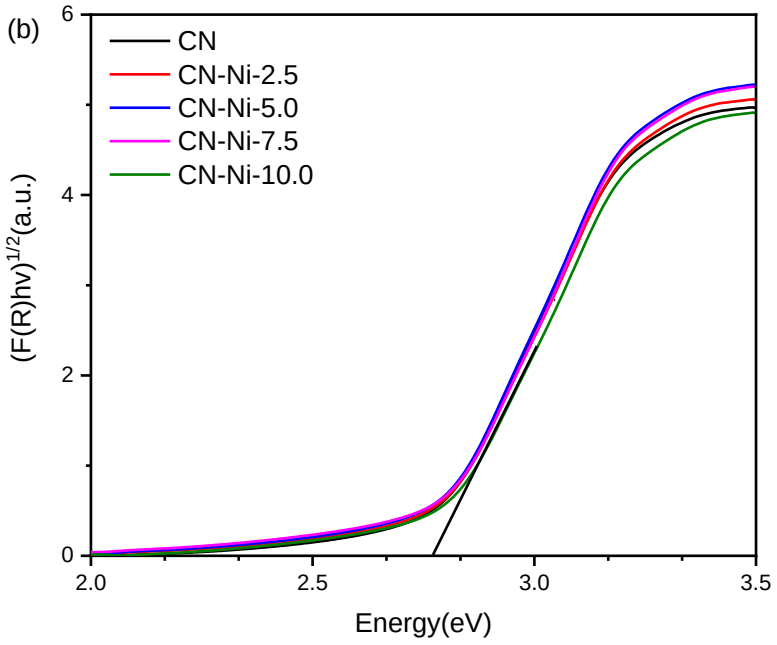

Figure 18 - (a) Diffuse reflectance spectra and (b) Kubelka-Munk plot for CN-Ni samples.

XRD pattern of CN and CN-Ni samples are shown in Figure 19, where all peaks of the XRD plot are in good agreement with hexagonal unit cell (a = b = 4.7420 Å, c = 6.7205 Å, α = β = 90°, γ = 120°) with space group P$\bar{6}$m2.[124] The XRD patterns for all the samples shows two major broad diffraction peaks at 13.1° and 27.3° that confirm their nanocrystalline or even amorphous nature. This is expected, ones CN is an organic semiconductor. The stronger peak at 27.3° could be indexed as diffraction plane (002), which is due to the interplanar stacking of aromatic systems with an interlayer distance d = 0.325 nm.[125] The peak at 13.1° corresponds to the (100) diffraction plane, which is put down to an in-planar structural packing motif with an intralayer distance of d = 0.663 nm.[125] These two characteristic diffraction peaks were consistent with the CN reported before.[126] The values of calculated interlayer and intralayer distance of CN-based samples are presented in Table 1.

Within the resolution of the XRD instrument and the technique itself, no identifiable reflection peaks associated with nickel species, including metallic nickel (Ni^0) and nickel oxide/hydroxide (NiO_x or $Ni(OH)_x$) can be observed in any of the Ni-deposited CN samples, even with longer deposition times. This is due the low amount of metal present in the sample, as indicated by ICP-OES and corroborating with SEM and EDS analyses. As the deposition

time increases, the overall peak intensity of the CN-Ni samples slightly decreases compared to the CN.

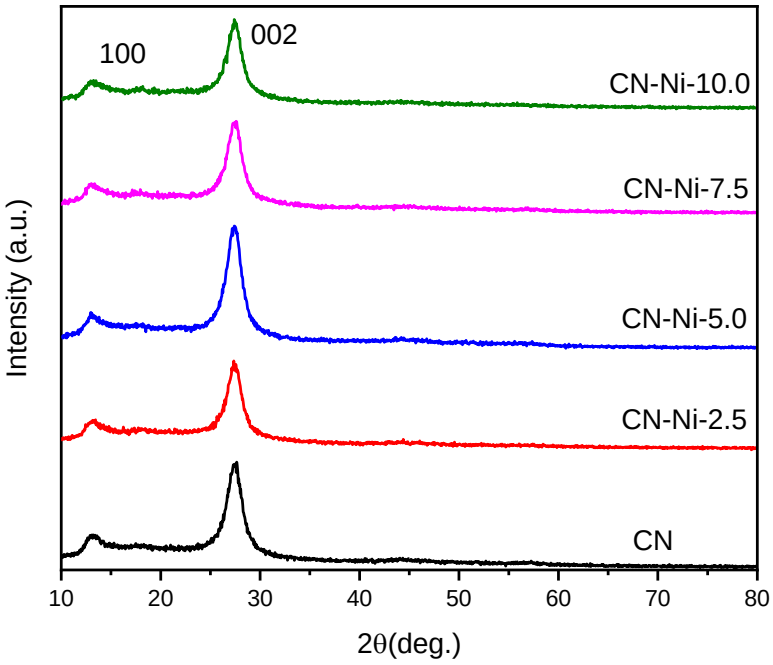

Figure 19 - XRD pattern of CN and CN-Ni samples.

Table 1 - Crystal parameters of CN-based samples obtained from XRD.

Sample	Interlayer distance (nm)	Intralayer distance (nm)
CN	0.325	0.663
CN-Ni-2.5	0.325	0.660
CN-Ni-5.0	0.325	0.669
CN-Ni-7.5	0.325	0.669
CN-Ni-10.0	0.325	0.664

The FTIR spectra of the synthesized CN and CN-Ni samples are shown in Figure 20. Two prominent peaks at 800 cm^{-1} and 882 cm^{-1} indicate the presence of s-triazine units, attributed to the out-of-plane bending vibrations of the triazine ring. The peaks at 1231 cm^{-1},

1315 cm^{-1}, 1398 cm^{-1}, 1460 cm^{-1}, and 1537 cm^{-1} correspond to the stretching vibrations of the C–N bonds in tri-s-triazine. The peak at 1626 cm^{-1} is associated with the stretching vibration of the C=N bond in the heptazine units. The broad absorption peak at 3152 cm^{-1} reflects the stretching vibration of the N–H bond in NH and NH_2 groups, likely due to incomplete polycondensation of CN.[127] As depicted in Figure 20, the FTIR spectra of CN and CN-Ni samples reveal the same chemical structure.

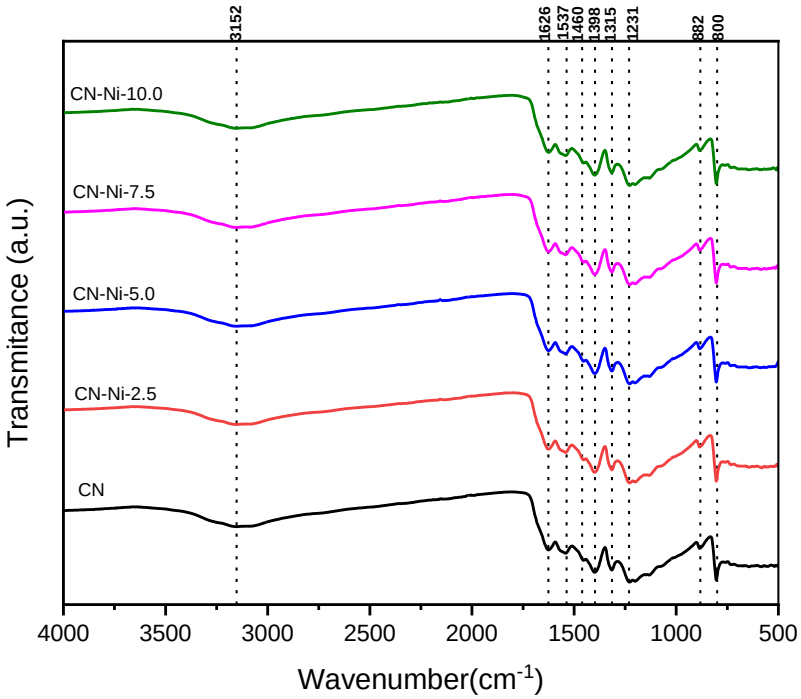

Figure 20 - FTIR spectra of the CN and CN-Ni samples.

XPS measurements were performed to investigate the chemical composition and oxidation states of the samples. Figure 21 displays the wide scan for all samples, highlighting the main peaks observed at 285 eV, 400 eV, 532 eV, and 855 eV, which correspond to C 1s, N 1s, O 1s, and Ni 2p, respectively. The oxygen species detected may be attributed to adventitious carbon molecules, which are inherently present when any surface is exposed to atmospheric conditions and to potential metal oxides. With increased deposition time, a slight increase in the Ni 2p signal is noted, which will be examined in further detail next. Overall, it shows no contamination or any other elements than expected based on the composition of the sample.

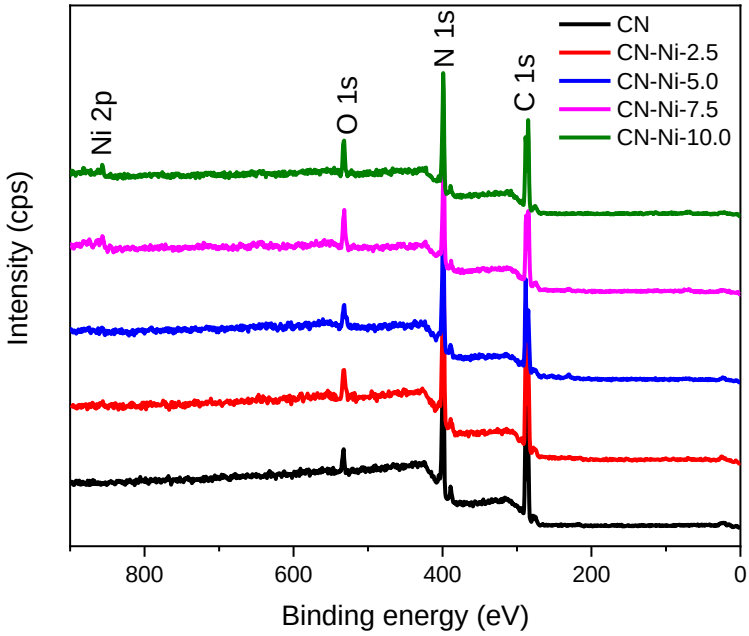

Figure 21 - Survey XPS spectra for CN-based samples.

This catalyst study here is rich in both carbon and nitrogen, making it essential to investigate their chemical environments to better understand its physicochemical properties. However, due to the inherent presence of adventitious carbon in any sample exposed to air, we focus the discussion on the N 1s signal to avoid misinterpretation of the C 1s spectra. Figure 22 shows the high-resolution signal of N 1s region, which was deconvoluted into four different components. These components have the binding energy of 398.7 eV, 399.6 eV, 400.5 eV, and 401.4 eV, which were assigned to C-N=C, C-NH_2, $(C)_2$-NH, and $(C)_3$-N.[128]

Additionally, when examining the amount of each component (Table 2), no significant changes (<2.1 at%) were observed in the $(C)_3$-N and $(C)_2$-NH components after Ni deposition. However, for the C-N=C and C-NH_2 components, a difference of ~11.1 at% was observed in both. This confirms that new chemical bonds were established on the photocatalyst after Ni deposition. Despite not having observed structural changes using XRD (bulk), the increased amount of C-NH_2 species suggests the presence of more “edges” in the CN surface. Given that the only difference between the samples is the amount of Ni, this change could be related to the interaction between the photocatalyst (CN) and the cocatalyst (Ni).

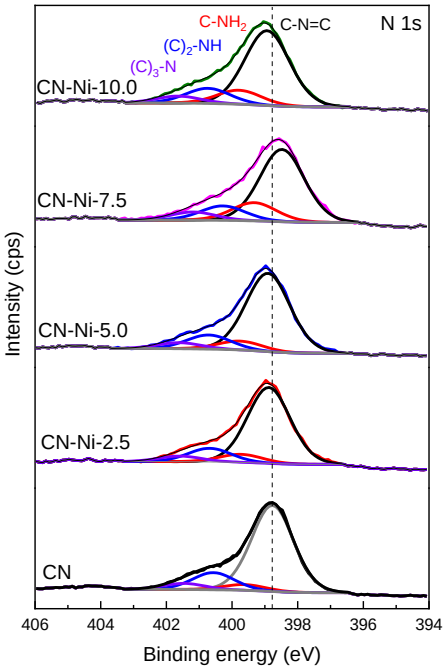

Figure 22 - N 1s XPS spectra for CN-based samples.

Table 2 - Amount of each component extracted from N 1s XPS spectra.

Sample	Component (%at)			
	C-N=C	**C-NH_2**	**$(C)_2$-NH**	**$(C)_3$-N**
CN	74.826	4.986	14.912	5.276
CN-Ni-2.5	73.538	7.854	13.21	5.399
CN-Ni-5.0	72.915	8.278	13.199	5.607
CN-Ni-7.5	63.892	16.09	12.817	7.201
CN-Ni-10.0	67.493	12.609	13.642	6.255

Aiming to understand the chemical environment of Ni deposited over CN, high-resolution XPS spectra measurements for Ni 2p region were made and the results are presented in Figure 23. We clearly observe an increase in intensity with the increasing of deposition time. It suggests a higher amount of %at Ni at the surface of CN. In addition, for

depositions times higher than 2.5 minutes, the spectra present two main Ni 2p peaks with energies corresponding to the Ni $2p_{3/2}$ and Ni $2p_{1/2}$ spin orbitals, along with the satellite peaks, confirming the presence of Ni species in the samples.

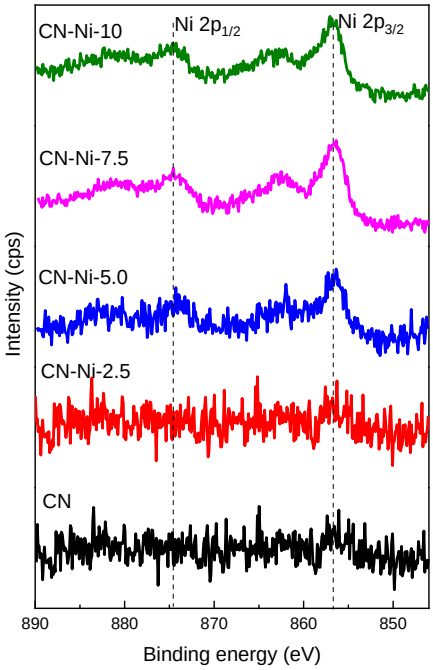

Figure 23 - Ni 2p XPS spectra for CN-based samples.

In order to better understand the chemical environment of CN-Ni samples, and given the reasonable signal-to-noise ratio for the samples CN-Ni-7.5 and CN-Ni-10.0, their components were investigated. As observed in Figure 24, it is possible to identify two Ni species: NiO at 855.3 eV and 872.8 eV related to Ni $2p_{3/2}$ and Ni $2p_{1/2}$, respectively; $Ni(OH)_2$ at 856.9 eV and 874.4 eV related to Ni $2p_{3/2}$ and Ni $2p_{1/2}$, respectively. Despite using as a precursor a target of metallic Ni (Ni^0), this analysis confirms that after the exposure of the sample to ambient conditions, there is the inevitable oxidation of the surface and the state of Ni in the samples becomes Ni^{2+}, forming a structure as NiO_x and/or $Ni(OH)_x$.[129] Interestingly, given two different species it may influence photocatalytic reactions. In addition, it is also observed a peak shift to higher binding energies with the increasing amount of Ni, which could be related to a change on the Fermi level of the samples.

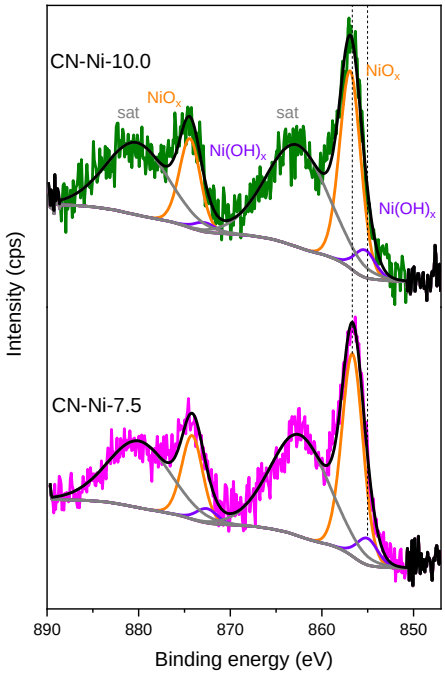

Figure 24 - Ni 2p XPS spectra for CN-Ni-7.5 and CN-Ni-10.0 samples.

XAS is a powerful technique for investigating the local electronic structure of materials. It was utilized to characterize the CN-based materials to better understand their unoccupied electronic states.

The C K-edge XAS spectra for the samples CN and CN-Ni-10.0 is presented in Figure 25. The C K-edge XAS spectra consist of contributions from transitions from 1s orbital to π* at the region from 285 to 290 eV, and σ* at 293–304 eV. The π* feature at ~286 eV is typical of the out-of-plane C=C bond, related to interlayer bonding. The variation in the shoulder at ~290 eV, attributed to carbon species in different carbon-oxygen functional groups, indicates differences between the samples. This could be related to the interaction of NiO_x and/or $Ni(OH)_x$ species with the photocatalyst.

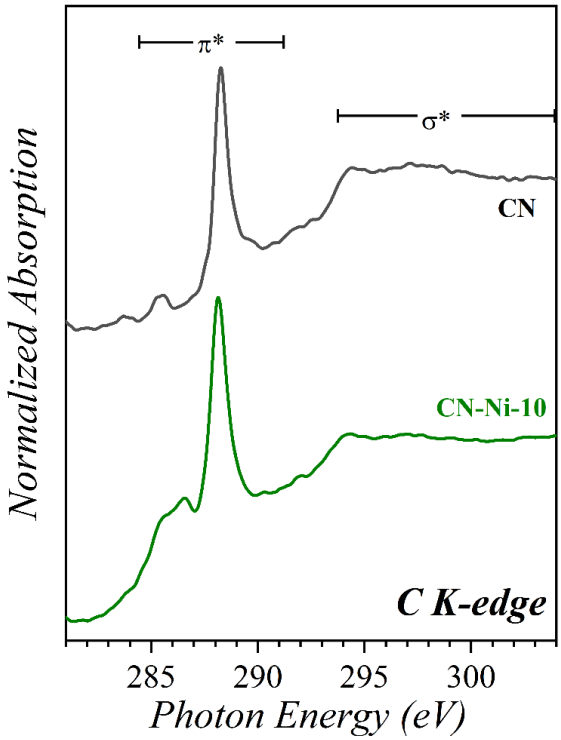

Figure 25 - C K-edge XAS spectra for CN and CN-Ni-10.0 samples.

In the N K-edge region (Figure 26), two main characteristic regions are observed, corresponding to the 1s → π* transition and the 1s → σ* transition. The most noticeable change occurs in the signal from graphitic three-fold nitrogen atoms (referred to as pyrrolic, related to C-NH_2 and $(C)_2$-NH), which slightly increases in intensity after Ni deposition. According to the XPS results, the component that showed increased atomic percentage was C-NH_2, not $(C)_2$-NH. Although no significant changes were observed in the N K-edge signal, our empirical evidence suggests that the C-NH_2 species are the ones undergoing modification. In addition, this finding is consistent with the observed change in the out-of-plane C=C bond from the C K-edge.

Overall, it seems that the tri-s-triazine moieties in the CN structure were well preserved even after Ni incorporation. Maintaining tri-s-triazine moieties could be beneficial in avoiding charge recombination at trap states when in a photocatalytic reaction.

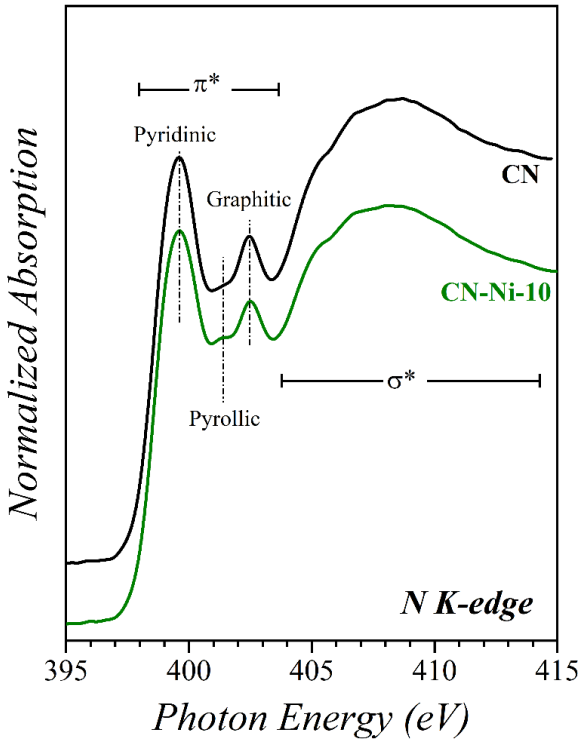

Figure 26 - N K-edge XAS spectra for CN and CN-Ni-10.0 samples.

In the Ni $L_{3,2}$-edge region (Figure 27), two main peaks are observed, corresponding to the Ni^{2+} oxidation state. It corroborates with the XPS results, when occupied energy levels were taken into consideration. It confirms the presence of NiO_x and $Ni(OH)_x$ species in the samples. A significant difference in intensity is also noted, which is related to the amount of Ni species present in the samples.

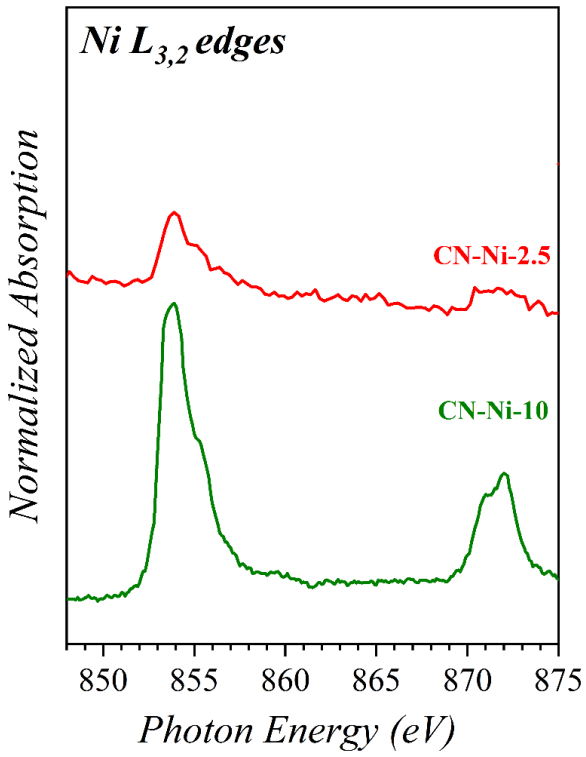

Figure 27 - Ni $L_{3,2}$-edge XAS spectra for CN-Ni-2.5 and CN-Ni-10.0 samples.

5.4. PHOTOCATALYTIC PERFORMANCE

With the deposition of Ni species on CN, the optical properties of the samples studied by UV-Vis spectroscopy remain very similar to pristine CN. It means that the energy required to excite an electron from VB to CB, for the studied samples, is $hv \geq 2.77\ eV$.

To further investigate the optoelectronic properties of the samples aiming a photocatalytic application for H_2 production, Figure 28 presents the XPS analysis of the VB region. The measured values are 1.51 eV, 1.76 eV, 1.77 eV, 1.69 eV, and 1.99 eV for CN, CN-Ni-2.5, CN-Ni-5.0, CN-Ni-7.5, and CN-Ni-10.0, respectively.

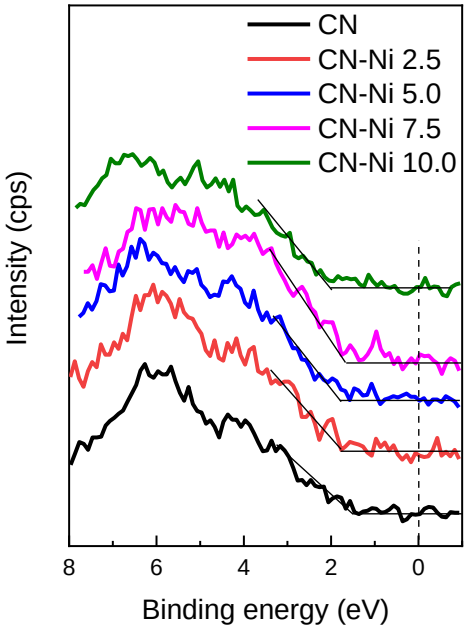

Figure 28 - VB XPS spectra for CN-based samples.

The CB values can be calculated using Equation 9:

$$VB = CB + E_{gap} \quad (9)$$

Where E_{gap} is the value extracted from UV-Vis spectroscopy, and VB is extracted from XPS. The calculated CB value of CN, CN-Ni-2.5, CN-Ni-5.0, CN-Ni-7.5, and CN-Ni-10.0 was -1.26 eV, -1.01 eV, -1.0 eV, -1.08 eV, and -0.78 eV, respectively. The calculated values are in accordance with literature.[130]

Thus, it allows us to construct the energy level diagram of the samples related to the oxidation (1.23 eV vs NHE, O_2/H_2O) and reduction (0 eV vs NHE, H^+/H_2) potentials of water (Figure 29). As shown in the band alignment, the VB of the CN-Ni-based samples exhibits a positive shift compared to that of CN, suggesting an enhanced oxidation ability.

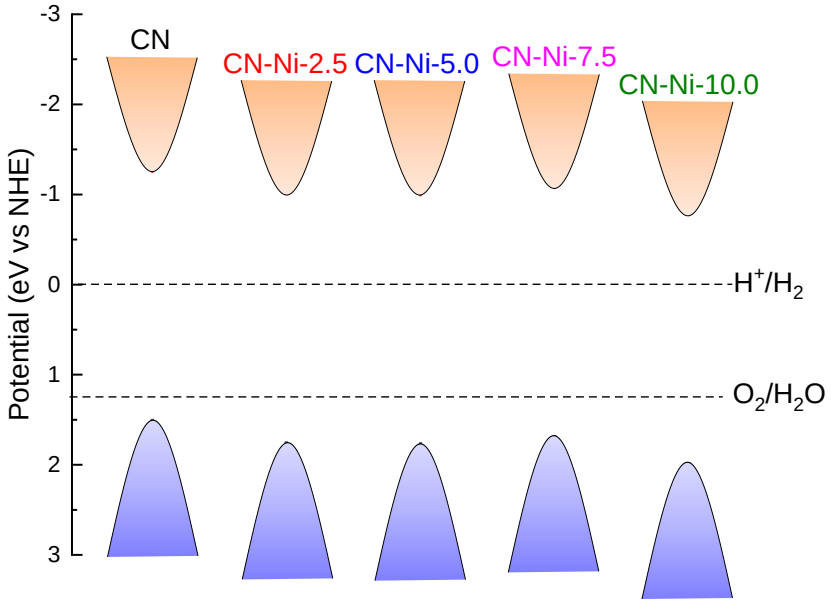

Figure 29 - Energy level diagram estimated for CN-based samples.

The reduction ability is not the only factor that affects the photocatalytic performance. The cocatalyst also play a key role, by promoting the charge separation, enhancing the stability of the photocatalyst, and increasing the active sites for the reaction. All those factors can lead to higher kinetics and enhanced activity.

The two Ni^{2+} species identified in the samples through XPS and XAS analysis, when used as cocatalysts for reactions such as water splitting, have different mechanisms. NiO is known and reported as a hole scavenger. Since NiO is a p-type semiconductor and CN is an n-type semiconductor, this structure can be treated as a p-n junction. Therefore, due to the formation of an electric field at the surface after charge equilibrium at the interface, the holes induced by radiation are driven towards the NiO structure. These holes can participate in oxidation reactions, such as water oxidation or the oxidation of a sacrificial agent.

On the other hand, $Ni(OH)_2$ is a commonly used cocatalyst for reduction reactions. Although different mechanisms and functions of $Ni(OH)_2$ can be found in the literature when employed in heterogeneous catalysis, one commonly accepted proposal is that the photogenerated electrons from the CB reduce $Ni(OH)_2$ species to Ni^0, where Ni^0 acts as an electron scavenger. For $Ni(OH)_2$ to work as a cocatalyst, the semiconductor acting as the

photocatalyst must have a reduction potential more negative than the reduction potential of $Ni(OH)_2/Ni^0$. This potential is reported as -0.23 V vs NHE (pH = 0).[131] Thus, the CN-Ni system is capable of using $Ni(OH)_2$ as a cocatalyst.

Thus, the photocatalytic activity of the samples in H_2 production will be tested using TEOA as a sacrificial agent to validate the assumptions made in this section. The aim is to elucidate the role of each species in the overall response to water reduction.

6. CONCLUSION

This study effectively highlighted the successful synthesis of CN and the application of magnetron sputtering to deposit Ni species as cocatalyst. Detailed physico-chemical investigations revealing the effects of Ni deposition on the structural and optoelectronic properties of the material. The study confirms that the target was made up of metallic nickel, and since reactive sputtering is not employed, XPS measurements indicate the presence of Ni^{2+} on the CN. The oxidation process is probably a result of either exposure to air or oxidation facilitated by the CN itself, and which can act as an effective cocatalyst, enhancing charge separation and can reduce the recombination, which are critical factors for the efficiency of photocatalytic processes. The incorporation of Ni also alters the chemical environment within the CN structure, which can be used to establish a mechanism involving photocatalytic H_2 production. These findings contribute to the broader understanding of semiconductor-cocatalyst interactions.

7. FUTURE PERSPECTIVES

To complete this research on Ni sputtered on CN for photocatalytic H_2 production, additional steps are necessary to elucidate the assumptions described throughout the thesis.

For instance, characterization techniques such as high-resolution transmission electron microscopy (HRTEM) could be used to evaluate the morphology of the cocatalyst and the presence of NiO_x/$Ni(OH)_x$ species. Additionally, fluorescence spectroscopy could be employed to investigate the recombination of charge carriers. X-ray absorption spectroscopy (XAS) data, including total electron yield (TEY) mode, have already been collected and require data processing.

These methods will provide detailed and concrete information about the size, distribution, and interaction of Ni species with CN, as well as help in understanding the electronic structure and chemical state of the Ni species in the composite. Furthermore, the photocatalytic activity of the samples for H_2 production using TEOA as a sacrificial agent is an ongoing step to evaluate the efficiency of the samples.

8. REFERENCES

1. Wang, Q. & Domen, K. Particulate Photocatalysts for Light-Driven Water Splitting: Mechanisms, Challenges, and Design Strategies. *Chem Rev* **120**, 919–985 (2020).

2. Qi, J., Zhang, W. & Cao, R. Solar-to-Hydrogen Energy Conversion Based on Water Splitting. *Adv Energy Mater* **8**, (2018).

3. Liu, G., Zhen, C., Kang, Y., Wang, L. & Cheng, H.-M. Unique physicochemical properties of two-dimensional light absorbers facilitating photocatalysis. *Chem Soc Rev* **47**, 6410–6444 (2018).

4. Niu, P. *et al.* Photocatalytic overall water splitting by graphitic carbon nitride. *InfoMat* **3**, 931–961 (2021).

5. Lin, L., Yu, Z. & Wang, X. Crystalline Carbon Nitride Semiconductors for Photocatalytic Water Splitting. *Angewandte Chemie* **131**, 6225–6236 (2019).

6. Yang, P., Ou, H., Fang, Y. & Wang, X. A Facile Steam Reforming Strategy to Delaminate Layered Carbon Nitride Semiconductors for Photoredox Catalysis. *Angewandte Chemie* **129**, 4050–4054 (2017).

7. Wen, J., Xie, J., Chen, X. & Li, X. A review on g-C 3 N 4 -based photocatalysts. *Appl Surf Sci* **391**, 72–123 (2017).

8. Liao, G. *et al.* Semiconductor polymeric graphitic carbon nitride photocatalysts: the “holy grail” for the photocatalytic hydrogen evolution reaction under visible light. *Energy Environ Sci* **12**, 2080–2147 (2019).

9. Wang, X. *et al.* A metal-free polymeric photocatalyst for hydrogen production from water under visible light. *Nat Mater* **8**, 76–80 (2009).

10. Martindale, B. C. M., Hutton, G. A. M., Caputo, C. A. & Reisner, E. Solar Hydrogen Production Using Carbon Quantum Dots and a Molecular Nickel Catalyst. *J Am Chem Soc* **137**, 6018–6025 (2015).

11. Duro, J. A., Lauk, C., Kastner, T., Erb, K. H. & Haberl, H. Global inequalities in food consumption, cropland demand and land-use efficiency: A decomposition analysis. *Global Environmental Change* **64**, 102124 (2020).

12. Hassan, A., Ilyas, S. Z., Jalil, A. & Ullah, Z. Monetization of the environmental damage caused by fossil fuels. *Environ Sci Pollut Res Int* **28**, 21204–21211 (2021).

13. Hutchins, D. A. *et al.* Climate change microbiology — problems and perspectives. *Nat Rev Microbiol* **17**, 391–396 (2019).

14. Flooding in Brazil - 2024 - PAHO/WHO | Pan American Health Organization. https://www.paho.org/en/health-emergencies/flooding-brazil-2024.

15. Asghar, U. *et al.* Review on the progress in emission control technologies for the abatement of CO2, SOx and NOx from fuel combustion. *J Environ Chem Eng* **9**, 106064 (2021).

16. San-Akca, B., Sever, S. D. & Yilmaz, S. Does natural gas fuel civil war? Rethinking energy security, international relations, and fossil-fuel conflict. *Energy Res Soc Sci* **70**, 101690 (2020).

17. Rahman, A., Farrok, O. & Haque, M. M. Environmental impact of renewable energy source based electrical power plants: Solar, wind, hydroelectric, biomass, geothermal, tidal, ocean, and osmotic. *Renewable and Sustainable Energy Reviews* **161**, 112279 (2022).

18. Hren, R. *et al.* Hydrogen production, storage and transport for renewable energy and chemicals: An environmental footprint assessment. *Renewable and Sustainable Energy Reviews* **173**, 113113 (2023).

19. Zohuri, B. The Chemical Element Hydrogen. *Hydrogen Energy* 1–35 (2019) doi:10.1007/978-3-319-93461-7_1.

20. Incer-Valverde, J., Korayem, A., Tsatsaronis, G. & Morosuk, T. “Colors” of hydrogen: Definitions and carbon intensity. *Energy Convers Manag* **291**, 117294 (2023).

21. Wietschel, M. & Ball, M. The hydrogen economy: Opportunities and challenges. *The Hydrogen Economy: Opportunities and Challenges* **9780521882163**, 1–646 (2009).

22. Joy, J., Mathew, J. & George, S. C. Nanomaterials for photoelectrochemical water splitting – review. *Int J Hydrogen Energy* **43**, 4804–4817 (2018).

23. Vincent, I. & Bessarabov, D. Low cost hydrogen production by anion exchange membrane electrolysis: A review. *Renewable and Sustainable Energy Reviews* **81**, 1690–1704 (2018).

24. Liu, J., Duan, X., Yuan, Z., Liu, Q. & Tang, Q. Experimental study on the performance, combustion and emission characteristics of a high compression ratio heavy-duty spark-ignition engine fuelled with liquefied methane gas and hydrogen blend. *Appl Therm Eng* **124**, 585–594 (2017).

25. Parra, D., Zhang, X., Bauer, C. & Patel, M. K. An integrated techno-economic and life cycle environmental assessment of power-to-gas systems. *Appl Energy* **193**, 440–454 (2017).

26. Zitelman, K. Potential State Regulatory Pathways to Facilitate Low-Carbon Fuels. (2022) doi:10.2172/1996418.

27. Bu, Y. & Ao, J. P. A review on photoelectrochemical cathodic protection semiconductor thin films for metals. *Green Energy & Environment* **2**, 331–362 (2017).

28. Maeda, K. & Domen, K. Photocatalytic Water Splitting: Recent Progress and Future Challenges. *J Phys Chem Lett* **1**, 2655–2661 (2010).

29. Joy, J., Mathew, J. & George, S. C. Nanomaterials for photoelectrochemical water splitting – review. *Int J Hydrogen Energy* **43**, 4804–4817 (2018).

30. Norkobilovich, K. I. Physical Basics of Semiconductors. *Texas Journal of Engineering and Technology* **26**, 1–5 (2023).

31. Conductors and Insulators: Definitions, Differences, Applications. https://testbook.com/physics/conductor-and-insulator.

32. Erkaboev, U. I., Gulyamov, G., Mirzaev, J. I. & Rakhimov, R. G. Modeling on the temperature dependence of the magnetic susceptibility and electrical conductivity oscillations in narrow-gap semiconductors. *https://doi.org/10.1142/S0217979220500526* **34**, (2020).

33. Lin, H., Xu, S., Zhang, Y. Q. & Wang, X. Electron transport and bulk-like behavior of wiedemann-franz law for sub-7 nm-thin iridium films on silkworm silk. *ACS Appl Mater Interfaces* **6**, 11341–11347 (2014).

34. Cao, W. & Cao, W. Semiconductor Photocatalysis - Materials, Mechanisms and Applications. *Semiconductor Photocatalysis - Materials, Mechanisms and Applications* (2016) doi:10.5772/61384.

35. Al-Madanat, O., AlSalka, Y., Ramadan, W. & Bahnemann, D. W. TiO2 Photocatalysis for the Transformation of Aromatic Water Pollutants into Fuels. *Catalysts* **11**, 317 (2021).

36. Jiang, C., Moniz, S. J. A., Wang, A., Zhang, T. & Tang, J. Photoelectrochemical devices for solar water splitting – materials and challenges. *Chem Soc Rev* **46**, 4645–4660 (2017).

37. (PDF) OPTIMIZATION OF NANOWIRE PHOTODIODE DEVICES FOR NEURONAL CELL SURVIVAL. https://www.researchgate.net/publication/263733837_OPTIMIZATION_OF_NANOWIRE_PHOTODIODE_DEVICES_FOR_NEURONAL_CELL_SURVIVAL.

38. Reddy, D. A., Liu, C., Vijayalakshmi, R. P. & Reddy, B. K. Effect of Al doping on the structural, optical and photoluminescence properties of ZnS nanoparticles. *J Alloys Compd* **582**, 257–264 (2014).

39. Balkan, N. & Erol, A. Intrinsic and Extrinsic Semiconductors. in 37–78 (2021). doi:10.1007/978-3-319-44936-4_2.

40. What are semiconductors? definition, types, industries. https://www.rs-online.com/designspark/what-are-semiconductors-definition-types-industries.

41. Chen, S., Takata, T. & Domen, K. Particulate photocatalysts for overall water splitting. *Nat Rev Mater* **2**, 17050 (2017).

42. Kudo, A. & Miseki, Y. Heterogeneous photocatalyst materials for water splitting. *Chem. Soc. Rev.* **38**, 253–278 (2009).

43. Chen, S., Takata, T. & Domen, K. Particulate photocatalysts for overall water splitting. *Nat Rev Mater* **2**, 17050 (2017).

44. Maeda, K. & Domen, K. Photocatalytic water splitting: Recent progress and future challenges. *Journal of Physical Chemistry Letters* **1**, 2655–2661 (2010).

45. Hisatomi, T., Takanabe, K. & Domen, K. Photocatalytic Water-Splitting Reaction from Catalytic and Kinetic Perspectives. *Catal Letters* **145**, 95–108 (2015).

46. Cao, S., Low, J., Yu, J. & Jaroniec, M. Polymeric Photocatalysts Based on Graphitic Carbon Nitride. *Advanced Materials* **27**, 2150–2176 (2015).

47. Zheng, Y., Lin, L., Wang, B. & Wang, X. Graphitic Carbon Nitride Polymers toward Sustainable Photoredox Catalysis. *Angewandte Chemie - International Edition* **54**, 12868–12884 (2015).

48. Hisatomi, T., Kubota, J. & Domen, K. Recent advances in semiconductors for photocatalytic and photoelectrochemical water splitting. *Chem. Soc. Rev.* **43**, 7520–7535 (2014).

49. Chen, X., Shen, S., Guo, L. & Mao, S. S. Semiconductor-based Photocatalytic Hydrogen Generation. *Chem Rev* **110**, 6503–6570 (2010).

50. Maeda, K. Z-Scheme Water Splitting Using Two Different Semiconductor Photocatalysts. *ACS Catal* **3**, 1486–1503 (2013).

51. Kudo, A. & Miseki, Y. Heterogeneous photocatalyst materials for water splitting. *Chem. Soc. Rev.* **38**, 253–278 (2009).

52. Zhang, G., Lan, Z.-A. & Wang, X. Surface engineering of graphitic carbon nitride polymers with cocatalysts for photocatalytic overall water splitting. *Chem Sci* **8**, 5261–5274 (2017).

53. Kato, H., Asakura, K. & Kudo, A. Highly Efficient Water Splitting into H $_2$ and O $_2$ over Lanthanum-Doped NaTaO $_3$ Photocatalysts with High Crystallinity and Surface Nanostructure. *J Am Chem Soc* **125**, 3082–3089 (2003).

54. Zhuang, Z. *et al.* MoB/g-C $_3$ N $_4$ Interface Materials as a Schottky Catalyst to Boost Hydrogen Evolution. *Angewandte Chemie International Edition* **57**, 496–500 (2018).

55. Zhang, Z. & Yates, J. T. Band Bending in Semiconductors: Chemical and Physical Consequences at Surfaces and Interfaces. *Chem Rev* **112**, 5520–5551 (2012).

56. Zhang, Z. & Yates, J. T. Band Bending in Semiconductors: Chemical and Physical Consequences at Surfaces and Interfaces. *Chem Rev* **112**, 5520–5551 (2012).

57. Zhang, Z. & Yates, J. T. Band Bending in Semiconductors: Chemical and Physical Consequences at Surfaces and Interfaces. *Chem Rev* **112**, 5520–5551 (2012).

58. JIANG, X. & FUJI, M. Non-Noble Nanoparticles Cocatalysts in TiO₂ for Photocatalytic Hydrogen Production from Water. A review. *Journal of the Japan Society of Powder and Powder Metallurgy* **70**, 203–212 (2023).

59. Kumar, A., Choudhary, P., Kumar, A., Camargo, P. H. C. & Krishnan, V. Recent Advances in Plasmonic Photocatalysis Based on TiO $_2$ and Noble Metal Nanoparticles for Energy Conversion, Environmental Remediation, and Organic Synthesis. *Small* **18**, 2101638 (2022).

60. Bai, S., Jiang, J., Zhang, Q. & Xiong, Y. Steering charge kinetics in photocatalysis: intersection of materials syntheses, characterization techniques and theoretical simulations. *Chem Soc Rev* **44**, 2893–2939 (2015).

61. Michaelson, H. B. The work function of the elements and its periodicity. *J Appl Phys* **48**, 4729–4733 (1977).

62. Maeda, K. *et al.* Photocatalytic Activities of Graphitic Carbon Nitride Powder for Water Reduction and Oxidation under Visible Light. *The Journal of Physical Chemistry C* **113**, 4940–4947 (2009).

63. Guo, Y. *et al.* A Rapid Microwave-Assisted Thermolysis Route to Highly Crystalline Carbon Nitrides for Efficient Hydrogen Generation. *Angewandte Chemie* **128**, 14913–14917 (2016).

64. Wang, Y., Yao, J., Li, H., Su, D. & Antonietti, M. Highly Selective Hydrogenation of Phenol and Derivatives over a Pd@Carbon Nitride Catalyst in Aqueous Media. *J Am Chem Soc* **133**, 2362–2365 (2011).

65. Cheng, N. *et al.* Au-Nanoparticle-Loaded Graphitic Carbon Nitride Nanosheets: Green Photocatalytic Synthesis and Application toward the Degradation of Organic Pollutants. *ACS Appl Mater Interfaces* **5**, 6815–6819 (2013).

66. Xu, Y.-S. & Zhang, W.-D. Ag/AgBr-Grafted Graphite-like Carbon Nitride with Enhanced Plasmonic Photocatalytic Activity under Visible Light. *ChemCatChem* **5**, 2343–2351 (2013).

67. Zhang, G., Lan, Z.-A. & Wang, X. Surface engineering of graphitic carbon nitride polymers with cocatalysts for photocatalytic overall water splitting. *Chem Sci* **8**, 5261–5274 (2017).

68. Chen, G. *et al.* Efficient and Stable Bifunctional Electrocatalysts Ni/Ni $_x$ M $_y$ (M = P, S) for Overall Water Splitting. *Adv Funct Mater* **26**, 3314–3323 (2016).

69. Indra, A. *et al.* Nickel as a co-catalyst for photocatalytic hydrogen evolution on graphitic-carbon nitride (sg-CN): what is the nature of the active species? *Chemical Communications* **52**, 104–107 (2016).

70. Chen, Z., Sun, P., Fan, B., Zhang, Z. & Fang, X. In Situ Template-Free Ion-Exchange Process to Prepare Visible-Light-Active g-C $_3$ N $_4$ /NiS Hybrid Photocatalysts with Enhanced Hydrogen Evolution Activity. *The Journal of Physical Chemistry C* **118**, 7801–7807 (2014).

71. Sun, C. *et al.* Enhanced activity of visible-light photocatalytic H 2 evolution of sulfur-doped g-C 3 N 4 photocatalyst via nanoparticle metal Ni as cocatalyst. *Appl Catal B* **235**, 66–74 (2018).

72. Liu, J. *et al.* Amorphous NiO as co-catalyst for enhanced visible-light-driven hydrogen generation over g-C 3 N 4 photocatalyst. *Appl Catal B* **222**, 35–43 (2018).

73. Yu, J., Wang, S., Cheng, B., Lin, Z. & Huang, F. Noble metal-free Ni(OH)2–g-C3N4 composite photocatalyst with enhanced visible-light photocatalytic H2-production activity. *Catal Sci Technol* **3**, 1782 (2013).

74. Wang, Z., Fan, J., Cheng, B., Yu, J. & Xu, J. Nickel-based cocatalysts for photocatalysis: Hydrogen evolution, overall water splitting and CO2 reduction. *Materials Today Physics* **15**, 100279 (2020).

75. Sun, C. *et al.* Enhanced activity of visible-light photocatalytic H 2 evolution of sulfur-doped g-C 3 N 4 photocatalyst via nanoparticle metal Ni as cocatalyst. *Appl Catal B* **235**, 66–74 (2018).

76. Hu, C.-C. & Teng, H. Structural features of p-type semiconducting NiO as a co-catalyst for photocatalytic water splitting. *J Catal* **272**, 1–8 (2010).

77. Xie, L. *et al.* Recent advances of nickel hydroxide-based cocatalysts in heterogeneous photocatalysis. *Catal Commun* **162**, 106371 (2022).

78. Zhou, Y., Lin, D., Ye, X. & Zhu, M. Facile synthesis of sulfur-doped Ni(OH)2 as an efficient co-catalyst for g-C3N4 in photocatalytic hydrogen evolution. *J Alloys Compd* **839**, 155691 (2020).

79. Kawai, T. & Sakata, T. Conversion of carbohydrate into hydrogen fuel by a photocatalytic process. *Nature 1980 286:5772* **286**, 474–476 (1980).

80. Schneider, J. & Bahnemann, D. W. Undesired Role of Sacrificial Reagents in Photocatalysis. *J Phys Chem Lett* **4**, 3479–3483 (2013).

81. Melián, E. P. *et al.* Efficient and affordable hydrogen production by water photo-splitting using TiO2-based photocatalysts. *Int J Hydrogen Energy* **38**, 2144–2155 (2013).

82. Wu, N. L. & Lee, M. S. Enhanced TiO2 photocatalysis by Cu in hydrogen production from aqueous methanol solution. *Int J Hydrogen Energy* **29**, 1601–1605 (2004).

83. Wu, N. L. & Lee, M. S. Enhanced TiO2 photocatalysis by Cu in hydrogen production from aqueous methanol solution. *Int J Hydrogen Energy* **29**, 1601–1605 (2004).

84. Kumaravel, V. *et al.* Photocatalytic Hydrogen Production: Role of Sacrificial Reagents on the Activity of Oxide, Carbon, and Sulfide Catalysts. *Catalysts 2019, Vol. 9, Page 276* **9**, 276 (2019).

85. Wang, M., Shen, S., Li, L., Tang, Z. & Yang, J. Effects of sacrificial reagents on photocatalytic hydrogen evolution over different photocatalysts. *J Mater Sci* **52**, 5155–5164 (2017).

86. Zhou, X., Li, Y., Xing, Y., Li, J. & Jiang, X. Effects of the preparation method of Pt/g-C_3N_4 photocatalysts on their efficiency for visible-light hydrogen production. *Dalton Transactions* **48**, 15068–15073 (2019).

87. Liang, Q. *et al.* Recent advances of melamine self-assembled graphitic carbon nitride-based materials: Design, synthesis and application in energy and environment. *Chemical Engineering Journal* **405**, 126951 (2021).

88. Teixeira, I., Quiroz, J., Homsi, M. & Camargo, P. An Overview of the Photocatalytic H2 Evolution by Semiconductor-Based Materials for Nonspecialists. *J Braz Chem Soc* (2020) doi:10.21577/0103-5053.20190255.

89. Wang, Z., Li, C. & Domen, K. Recent developments in heterogeneous photocatalysts for solar-driven overall water splitting. *Chem Soc Rev* **48**, 2109–2125 (2019).

90. Maeda, K. & Domen, K. New Non-Oxide Photocatalysts Designed for Overall Water Splitting under Visible Light. *The Journal of Physical Chemistry C* **111**, 7851–7861 (2007).

91. Matsumura, M., Saho, Y. & Tsubomura, H. Photocatalytic hydrogen production from solutions of sulfite using platinized cadmium sulfide powder. *J Phys Chem* **87**, 3807–3808 (1983).

92. Chen, X., Shen, S., Guo, L. & Mao, S. S. Semiconductor-based Photocatalytic Hydrogen Generation. *Chem Rev* **110**, 6503–6570 (2010).

93. Anjumol, K. S. *et al.* Graphitic carbon nitride-based nanocomposites. in *Synthesis, Characterization, and Applications of Graphitic Carbon Nitride* 59–76 (Elsevier, 2023). doi:10.1016/B978-0-12-823038-1.00003-9.

94. Murali, A., Sakar, M., Priya, S., Bensingh, R. J. & Kader, M. A. Graphitic-Carbon Nitride for Hydrogen Storage. in *Nanoscale Graphitic Carbon Nitride* 487–514 (Elsevier, 2022). doi:10.1016/B978-0-12-823034-3.00017-0.

95. LIEBIG, J. Uber einige Stickstoff - Verbindungen. *Annalen der Pharmacie* **10**, 1–47 (1834).

96. Franklin, E. C. THE AMMONO CARBONIC ACIDS. *J Am Chem Soc* **44**, 486–509 (1922).

97. Pauling, L. & Sturdivant, J. H. The Structure of Cyameluric Acid, Hydromelonic Acid and Related Substances. *Proceedings of the National Academy of Sciences* **23**, 615–620 (1937).

98. Redemann, C. E. & Lucas, H. J. Some Derivatives of Cyameluric Acid and Probable Structures of Melam, Melem and Melon. *J Am Chem Soc* **62**, 842–846 (1940).

99. Wang, C.-Y., Maeda, K., Chang, L.-L., Tung, K.-L. & Hu, C. Synthesis and applications of carbon nitride (CN) family with different carbon to nitrogen ratio. *Carbon N Y* **188**, 482–491 (2022).

100. Cui, Y. *et al.* Synthesis of bulk and nanoporous carbon nitride polymers from ammonium thiocyanate for photocatalytic hydrogen evolution. *J Mater Chem* **21**, 13032 (2011).

101. Kumar, S., Battula, V. R. & Kailasam, K. Single molecular precursors for CxNy materials- Blending of carbon and nitrogen beyond g-C3N4. *Carbon N Y* **183**, 332–354 (2021).

102. LIEBIG, J. Uber einige Stickstoff - Verbindungen. *Annalen der Pharmacie* **10**, 1–47 (1834).

103. Franklin, E. C. The ammono carbonic acids. *J Am Chem Soc* **44**, 486–509 (1922).

104. Kroke, E. & Schwarz, M. Novel group 14 nitrides. *Coord Chem Rev* **248**, 493–532 (2004).

105. Kroke, E. *et al.* Tri-s-triazine derivatives. Part I. From trichloro-tri-s-triazine to graphitic C3N4 structuresPart II: Alkalicyamelurates M3[C6N7O3], M = Li, Na, K, Rb, Cs, manuscript in preparation. *New Journal of Chemistry* **26**, 508–512 (2002).

106. Komatsu, T. & Nakamura, T. Polycondensation/pyrolysis of tris-s-triazine derivatives leading to graphite-like carbon nitrides. *J Mater Chem* **11**, 474–478 (2001).

107. Parvez, K. Two-Dimensional Nanomaterials: Crystal Structure and Synthesis. in *Biomedical Applications of Graphene and 2D Nanomaterials* 1–25 (Elsevier, 2019). doi:10.1016/B978-0-12-815889-0.00001-5.

108. Phoon, B. L. *et al.* Co-Doped, Tri-Doped, and Rare-Earth-Doped g-C3N4 for Photocatalytic Applications: State-of-the-Art. *Catalysts* **12**, (2022).

109. Appaturi, J. N. *et al.* A review of the recent progress on heterogeneous catalysts for Knoevenagel condensation. *Dalton Transactions* **50**, 4445–4469 (2021).

110. Thomas, A. *et al.* Graphitic carbon nitride materials: variation of structure and morphology and their use as metal-free catalysts. *J Mater Chem* **18**, 4893 (2008).

111. (PDF) Synthesis, characterization, and performance of g-C3N4 based materials decorated with Au nanoparticles for (photo) catalytic applications. https://www.researchgate.net/publication/336898971_Synthesis_characterization_and_performance_of_g-

C3N4_based_materials_decorated_with_Au_nanoparticles_for_photo_catalytic_applications.

112. Ong, W.-J., Tan, L.-L., Ng, Y. H., Yong, S.-T. & Chai, S.-P. Graphitic Carbon Nitride (g-C_3N_4)-Based Photocatalysts for Artificial Photosynthesis and Environmental Remediation: Are We a Step Closer To Achieving Sustainability? *Chem Rev* **116**, 7159–7329 (2016).

113. Wang, X. *et al.* A metal-free polymeric photocatalyst for hydrogen production from water under visible light. *Nat Mater* **8**, 76–80 (2009).

114. Jürgens, B. *et al.* Melem (2,5,8-Triamino-tri- *s* -triazine), an Important Intermediate during Condensation of Melamine Rings to Graphitic Carbon Nitride: Synthesis, Structure Determination by X-ray Powder Diffractometry, Solid-State NMR, and Theoretical Studies. *J Am Chem Soc* **125**, 10288–10300 (2003).

115. Kroke, E. *et al.* Tri-s-triazine derivatives. Part I. From trichloro-tri-s-triazine to graphitic C3N4 structuresPart II: Alkalicyamelurates M3[C6N7O3], M = Li, Na, K, Rb, Cs, manuscript in preparation. *New Journal of Chemistry* **26**, 508–512 (2002).

116. Li, J. *et al.* Achieving Efficient Incorporation of π-Electrons into Graphitic Carbon Nitride for Markedly Improved Hydrogen Generation. *Angewandte Chemie* **131**, 2007–2011 (2019).

117. Li, K., Su, F.-Y. & Zhang, W.-D. Modification of g-C3N4 nanosheets by carbon quantum dots for highly efficient photocatalytic generation of hydrogen. *Appl Surf Sci* **375**, 110–117 (2016).

118. Liao, G. *et al.* Semiconductor polymeric graphitic carbon nitride photocatalysts: the “holy grail” for the photocatalytic hydrogen evolution reaction under visible light. *Energy Environ Sci* **12**, 2080–2147 (2019).

119. Cheng, C. *et al.* Electrogenerated Chemiluminescence Behavior of Graphite-like Carbon Nitride and Its Application in Selective Sensing Cu^{2+}. *Anal Chem* **84**, 4754–4759 (2012).

120. Gotipamul, P. P. *et al.* Impact of piezoelectric effect on the heterogeneous visible photocatalysis of g-C3N4/Ag/ZnO tricomponent. *Chemosphere* **287**, 132298 (2022).

121. Xu, Y. & Xu, R. Nickel-based cocatalysts for photocatalytic hydrogen production. *Appl Surf Sci* **351**, 779–793 (2015).

122. Shen, R. *et al.* Ni-based photocatalytic H2-production cocatalysts2. *Chinese Journal of Catalysis* **40**, 240–288 (2019).

123. Ahmed Shah Bukhari, S. *et al.* Development of Nickel doped Graphitic Carbon Nitride (GCN) Photocatalyst for Enhanced Degradation of textile pollutant under Visible Light Irradiation. *Journal of Saudi Chemical Society* 101801 (2023) doi:10.1016/j.jscs.2023.101801.

124. Fina, F., Callear, S. K., Carins, G. M. & Irvine, J. T. S. Structural Investigation of Graphitic Carbon Nitride via XRD and Neutron Diffraction. *Chemistry of Materials* **27**, 2612–2618 (2015).

125. Xin, G., Chemistry, Y. M.-J. of & 2013, undefined. Pyrolysis Synthesized gC3N4 for Photocatalytic Degradation of Methylene Blue. *hindawi.comG Xin, Y MengJournal of Chemistry, 2013•hindawi.com*.

126. Liu, F. *et al.* Ternary PVDF-based terpolymer nanocomposites with enhanced energy density and high power density. *Elsevier*.

127. Kotbi, A. *et al.* Gas Sensors Based on Exfoliated g-C3N4 for CO2 Detection. *Chemosensors* **10**, 470 (2022).

128. Alwin, E., Nowicki, W., Wojcieszak, R., Zieliński, M. & Pietrowski, M. Elucidating the structure of the graphitic carbon nitride nanomaterials *via* X-ray photoelectron spectroscopy and X-ray powder diffraction techniques. *Dalton Transactions* **49**, 12805–12813 (2020).

129. Deng, P. *et al.* Nickel formate induced high-level *in situ* Ni-doping of g-C $_3$ N $_4$ for a tunable band structure and enhanced photocatalytic performance. *J Mater Chem A Mater* **7**, 22385–22397 (2019).

130. Meng, N. *et al.* Engineering oxygen-containing and amino groups into two-dimensional atomically-thin porous polymeric carbon nitrogen for enhanced photocatalytic hydrogen production. *Energy Environ Sci* **11**, 566–571 (2018).

131. Chen, W., Zhang, M., Yang, S., Chen, J. & Tang, L. Ni(OH) $_2$ -modified SrTiO $_3$ for enhanced photocatalytic hydrogen evolution reactions. *New Journal of Chemistry* **44**, 7194–7199 (2020).